

# THE STELLAR MASS DENSITY AND SPECIFIC STAR FORMATION RATES OF THE UNIVERSE AT $Z \sim 7$

VALENTINO GONZÁLEZ<sup>1</sup>, IVO LABBÉ<sup>2</sup>, RYCHARD J. BOUWENS<sup>1,3</sup>, GARTH ILLINGWORTH<sup>1</sup>, MARIJN FRANX<sup>3</sup>, MARISKA KRIEK<sup>4</sup>,  
GABRIEL B. BRAMMER<sup>5</sup>

*Draft version November 5, 2018*

## ABSTRACT

We use a robust sample of 11  $z \sim 7$  galaxies ( $z_{850}$ -dropouts) to estimate the stellar mass density of the universe when it was only  $\sim 750$  Myr old. We combine the very deep optical to near-Infrared photometry from the HST ACS and NICMOS cameras with mid-Infrared Spitzer IRAC imaging available through the GOODS program. After carefully removing the flux from contaminating foreground sources we have obtained reliable photometry in the  $3.6 \mu\text{m}$  and  $4.5 \mu\text{m}$  IRAC channels. The spectral shapes of these sources, including their rest frame optical colors, strongly support their being at  $z \sim 7$  with a mean photometric redshift of  $\langle z \rangle = 7.2 \pm 0.5$ . We use Bruzual & Charlot (2003) synthetic stellar population models to constrain their stellar masses and star formation histories. We find stellar masses that range over  $0.1 - 12 \times 10^9 M_{\odot}$  and average ages from 20 Myr to up to 425 Myr with a mean of  $\sim 300$  Myr, suggesting that in some of these galaxies most of the stars were formed at  $z > 8$  (and probably at  $z \gtrsim 10$ ). The best fits to the observed SEDs are consistent with little or no dust extinction, in agreement with recent results at  $z \sim 4 - 8$ . The star formation rates (SFR) are in the range from  $5\text{-}20 M_{\odot} \text{ yr}^{-1}$ . From this sample we measure a stellar mass density of  $6.6_{-3.3}^{+5.4} \times 10^5 M_{\odot} \text{ Mpc}^{-3}$  to a limit of  $M_{UV,AB} < -20$  (or  $0.4L_{z=3}^*$ ). Combined with a fiducial lower limit for their ages (80 Myr) this implies a maximum SFR density of  $0.008 M_{\odot} \text{ yr}^{-1} \text{ Mpc}^{-3}$ . This is well below the critical level needed to reionize the universe at  $z \sim 8$  using standard assumptions. However, this result is based on luminous sources ( $>L^*$ ) and does not include the dominant contribution of the fainter galaxies. Strikingly, we find that the specific SFR is constant from  $z \sim 7$  to  $z \sim 2$  but drops substantially at more recent times.

*Subject headings:* galaxies: evolution — galaxies: high-redshift

## 1. INTRODUCTION

Direct observations of galaxies at high redshift from complete, well-defined searches place strong constraints on galaxy formation and evolution models. Extensive studies have been made of galaxies selected by the dropout technique out to redshift 6 (see e.g., Stanway et al. 2003; Bunker et al. 2004; Yan & Windhorst 2004; Bouwens et al. 2006, 2007; McLure et al. 2009a) thanks in part to the capabilities of the HST ACS and NICMOS cameras. Studies at higher redshifts, however, have been much more challenging. In particular, one of the key issues has been the derivation of stellar masses. These masses can provide both strong additional constraints on formation models and information about the star formation rates at even earlier times, effectively opening a window towards the earliest phases of galaxy formation. Deriving masses at higher redshifts does however face some distinct challenges.

At redshifts  $z > 4$ , ACS and NICMOS only access the rest-frame UV continuum, which is not a reliable tracer of stellar mass. To obtain better constraints on this quantity through SED fits it is necessary to ex-

tend the observations to the rest-frame optical. Although Spitzer data presents challenges due to its large instrumental PSF, these rest-frame optical measurements can be made at high redshifts with the  $3.6 \mu\text{m}$  and  $4.5 \mu\text{m}$  IR channels of the IRAC camera (Fazio et al. 2004). The IRAC  $3.6 \mu\text{m}$  and  $4.5 \mu\text{m}$  bands probe the rest-frame optical fluxes around  $0.5 - 0.6 \mu\text{m}$  of  $z \sim 5+$  sources and reach to  $\gtrsim 26$  AB mag at  $5\sigma$  in deep  $\gtrsim 23$  hr integrations. This is a remarkable achievement for a 0.8-m telescope. Spitzer will continue to play a unique role in the determination of fundamental properties like ages and stellar masses of the earliest galaxies until JWST is launched. These Spitzer and HST data have permitted estimates of stellar masses for large numbers ( $\gtrsim 150$ ) of  $z \sim 5\text{-}6$  sources (Yan et al. 2005; Eyles et al. 2005; Egami et al. 2005; Yan et al. 2006; Stark et al. 2009; Mobasher et al. 2005; Bradley et al. 2008; Zheng et al. 2009). One surprising early finding was the number of quite massive  $\sim 10^{10} M_{\odot}$  galaxies in  $z \sim 6$  samples (e.g. Yan et al. 2005; Eyles et al. 2005). It suggested that  $z \sim 5 - 6$  galaxies exhibited substantial amounts of star formation at much higher redshifts and earlier times, well into the epoch of reionization (Stark et al. 2007; Yan et al. 2006).

These analyses have also opened the possibility of looking at the SFR-Mass relation at higher redshifts, or equivalently, at the specific SFR or SSFR (i.e., SFR/Mass). The SSFR tells us how fast galaxies are growing with respect to their current stellar masses. While at low redshifts ( $0 < z < 1$ ) it has been shown that galaxies grew faster in earlier times than they do today (Noeske et al. 2007), it has been suggested that

<sup>1</sup> Astronomy Department, University of California, Santa Cruz, CA 95064

<sup>2</sup> Carnegie Observatories, 813 Santa Barbara Street, Pasadena, CA 91101

<sup>3</sup> Leiden Observatory, Leiden University, NL-2300 RA Leiden, Netherlands

<sup>4</sup> Department of Astrophysical Sciences, Princeton University, Princeton, NJ 08544

<sup>5</sup> Department of Astronomy, Yale University, New Haven, CT 06520

at higher redshift ( $4 < z < 6$ ) the SFR-Mass relation remains much more constant (Stark et al. 2009). This transition in the SSFR is an interesting and important result and needs to be assessed over a long redshift baseline.

It is imperative then to try to extend these studies to  $z \geq 7$  and investigate what are the characteristics of the probable progenitors of these rather massive  $z \sim 6$  sources. Doing so, however, has been challenging due to the difficulty in obtaining deep enough near-IR and optical data to robustly identify  $z \sim 7$  sources. Such sources only start to become “common” at  $\gtrsim 26.5$  AB mag. Thus, early selections of  $z \sim 7$   $z$ -dropouts from the HUDF only included a handful of candidates, and the situation has only improved slowly (Bouwens et al. 2004c, 2008; Oesch et al. 2009b). Consequently, very little has been published on the stellar masses of  $z \sim 7$   $z$ -dropout galaxies (Egami et al. 2005; Labbé et al. 2006). Labbé et al. (2006) performed stellar population modeling of four ACS  $z_{850}$ -band dropout sources found in the HUDF, and derived stellar masses of  $\sim 10^9 - 10^{10} M_{\odot}$ , ages of  $\sim 100$ -200 Myr, and was able to estimate a stellar mass density of  $1.6 \times 10^6 M_{\odot} \text{ Mpc}^{-3}$  (to  $0.3L_{z=3}^*$ ).

Fortunately, as a result of continued efforts to select  $z \sim 7$  galaxies from the growing quantity of deep near-IR NICMOS data, Bouwens et al. (2009, in preparation) have succeeded in substantially expanding the size of current  $z \sim 7$   $z$ -dropout selections, and now 14 NICMOS-selected, rather luminous  $z \sim 7$   $z$ -dropout galaxies are known that are amenable to stellar mass estimates. The recent advent of WFC3 on HST has expanded the number of known  $z \sim 7$  sources and now  $\sim 25$  sources are known at  $z \sim 7$  (Oesch et al. 2009a; Bouwens et al. 2009b; McLure et al. 2009b; Bunker et al. 2009; Castellano et al. 2009; Yan et al. 2009; Ouchi et al. 2009; Hickey et al. 2009; Wilkins et al. 2009). Most of the newly discovered galaxies, however, are too faint to attempt stellar mass estimations on individual basis, although valuable information can be obtained from these samples through stacking analysis (see Labbe et al. 2010<sup>6</sup>). Galaxies in the Bouwens et al. (2009, in preparation) sample extend from  $\sim 25.5$  AB mag to  $\sim 27.8$  AB mag and are found in the HUDF, and in and around the two wide-area GOODS fields. These candidates also possess very deep  $\gtrsim 23.3$  hr coverage with IRAC from the Spitzer GOODS program and present us with a unique opportunity to better understand what the typical properties (ages, stellar masses) of  $z \sim 7$   $z$ -dropouts are.

Here we take advantage of the larger sample of 14  $z_{850}$ -dropout sources identified by Bouwens et al. (2009, in preparation) to estimate the typical properties of  $z \sim 7$  galaxies. The much larger size of current samples allows us to get a better handle on the typical properties of  $z \sim 7$  galaxies than was possible from the smaller and brighter samples previously available (Labbé et al. 2006). For example, sizeable variations in the M/L ratios of individual galaxies can considerably skew the averages for the population as a whole. The present sample

also include galaxies from two independent lines of sight, i.e., the HDF-North GOODS and CDF-South GOODS, so the results should be much less impacted by cosmic variance and more representative of the cosmic average. In estimating the rest-frame optical fluxes for our  $z \sim 7$  candidates from the IRAC, we will take advantage of the well-tested deblending process described by Labbé et al. (2006) (see also Wuyts et al. 2007) which enables us to estimate fluxes when there is moderate overlap with nearby sources. This also allows for a larger sample, since the well-known problems with blending and confusion in IRAC data have limited previous studies.

We provide a brief outline for this paper here. We present the sample selection and observational data we have used in this work in §2 and §3 respectively. In §4, we will describe the photometry of the sample with particular emphasis in the deblended photometry from the IRAC channels. We devote §5 to a discussion of the photometric redshifts obtained and possible contamination and in §6 we present the procedure and results in the process of fitting synthetic stellar populations to the observed SEDs (including our SSFR results). §7 presents our estimated stellar mass density (SMD) at  $z \sim 7$  and confidence intervals. We compare our results to previous work in §8 and present a discussion of them in §9. We summarize our conclusions in §10. All magnitudes quoted in the paper are in the AB system (Oke & Gunn 1983). We have used cosmological parameters  $\Omega_{\Lambda} = 0.7$ ,  $\Omega_M = 0.3$  and  $H_0 = 70 \text{ kms s}^{-1} \text{ Mpc}^{-1}$  to facilitate comparison to previous works.

## 2. SAMPLE SELECTION

The present selection of  $z \sim 7$   $z$ -dropout candidates is based upon  $\sim 80 \text{ arcmin}^2$  of very deep optical ACS, near-IR NICMOS, and IRAC data available over and around the two GOODS fields – including the HUDF and HDF-North (see §3 for a more detailed description of these data). This selection is described in Bouwens et al. (2009, in preparation).

Candidates  $z \sim 7$  galaxies were required to satisfy a two-color Lyman-Break Galaxy (LBG) criterion adapted to  $z \sim 7$  – showing a strong  $z - J$  break but possessing a blue  $J - H$  color (redward of the break). In detail, the color criterion used is:

$$(z_{850} - J_{110})_{AB} > 0.8 \\ \wedge (z_{850} - J_{110})_{AB} > 0.8 + 0.4(J_{110} - H_{160})_{AB}$$

where  $\wedge$  represents the logical **AND** operation and where the colors were measured in a  $\sim 0.4''$ -diameter aperture using *SExtractor* in double image mode with the  $H_{160}$  band image being the detection image. Candidate  $z \gtrsim 7$  sources were also required to be undetected to less than  $2\sigma$  in the optical ACS bands ( $B_{435}$ ,  $V_{606}$ , and  $i_{775}$ ). Sources were also removed from the sample if they were detected at  $1.5\sigma$  in two or more of the optical bands. Only detections of at least  $5\sigma$  in the  $H_{160}$ -band images (measured in apertures of  $0.6''$  in diameter) were considered to ensure that our candidates corresponded to real sources. The candidates –with GNS IDs– were also required to have have ( $H_{160} - 5.8 \mu\text{m}$ ) colors bluer than 2.5 ( $5.8 \mu\text{m}$  photometry measured in  $2''$  diameter apertures). This provided added confidence that the sources were not low-redshift interlopers.

<sup>6</sup> The Labbe et al. (2010) work focuses exclusively on the ultra-faint, sub- $L^*$  sources. Only sources UDF-387-1125 and UDF-3244-4727 from this work (our faintest  $z_{850}$ -dropouts in the UDF) are also included in Labbe et al. (2010).

TABLE 1  
SUMMARY OF AVAILABLE DATA.

Filter	Depth [1 $\sigma$ ]	Reference
HUDF		
ACS - $B_{435}$	29.9	[1]
ACS - $v_{606}$	30.4	[1]
ACS - $i_{775}$	29.9	[1]
ACS - $z_{850}$	29.4	[1]
NICMOS - $J_{110}$	28.7	[5, 6]
NICMOS - $H_{160}$	28.3	[5, 6]
ISAAC - $K_s$	27.3	[11]
IRAC - $3.6\mu m$	27.5	[15]
IRAC - $4.5\mu m$	26.8	[15]
IRAC - $5.8\mu m$	25.8	[15]
IRAC - $8.0\mu m$	25.7	[15]
GOODS South		
ACS - $B_{435}$	28.8	[2, 3]
ACS - $v_{606}$	29.1	[2, 3]
ACS - $i_{775}$	28.5	[2, 3]
ACS - $z_{850}$	28.3	[2, 3]
NICMOS - $J_{110}$	28.0	[7, 8]
NICMOS - $H_{160}$	27.9	[7, 8]
IRAC - $3.6\mu m$	27.2	[15]
IRAC - $4.5\mu m$	26.4	[15]
IRAC - $5.8\mu m$	25.4	[15]
IRAC - $8.0\mu m$	25.3	[15]
GOODS North		
ACS - $B_{435}$	28.7	[2, 3]
ACS - $v_{606}$	29.0	[2, 3]
ACS - $i_{775}$	28.6	[2, 3]
ACS - $z_{850}$	28.5	[2, 3]
NICMOS - $J_{110}$	27.8	[7, 8]
NICMOS - $H_{160}$	27.7	[7, 8]
MOIRCS - $J_s$	27.1 <sup>a</sup>	[12, 13, 14]
MOIRCS - $K_s$	27.4 <sup>a</sup>	[12, 13, 14]
IRAC - $3.6\mu m$	27.2	[15]
IRAC - $4.5\mu m$	26.4	[15]
IRAC - $5.8\mu m$	25.4	[15]
IRAC - $8.0\mu m$	25.3	[15]
HDFN <sup>b</sup>		
ACS - $B_{435}$	29.2	[2, 3]
WFPC2 - $B'_{450}$	30.2	[4]
ACS - $v_{606}$	29.4	[2, 3]
WFPC2 - $v'_{606}$	29.0	[4]
ACS - $i_{775}$	28.6	[2, 3]
WFPC2 - $I_{814}$	28.8	[4]
ACS - $z_{850}$	28.23	[2, 3]
NICMOS - $J_{110}$	27.9	[9, 10]
NICMOS - $H_{160}$	28.1	[9, 10]
MOIRCS - $K_s$	27.6	[12, 13, 14]
IRAC - $3.6\mu m$	26.8	[15]
IRAC - $4.5\mu m$	26.2	[15]
IRAC - $5.8\mu m$	25.8	[15]
IRAC - $8.0\mu m$	25.7	[15]

REFERENCES. — (1) Beckwith et al. 2006; (2) Giavalisco et al. 2004; (3) Bouwens et al. 2007; (4) Williams et al. 1996; (5) Thompson et al. 2005; (6) Oesch et al. 2009b; (7) Conselice et al. 2009, in preparation; (8) Bouwens et al. 2009, in preparation; (9) Thompson et al. 1999; (10) Dickinson 1999; (11) Labbé et al. 2003; (12) Kajisawa et al. 2006; (13) Ouchi et al. 2007; (14) Bouwens et al. 2008; (15) Dickinson et al. 2009, in preparation

NOTE. — The depths of the data in the different fields. Optical to NIR were estimated using  $0.9''$  diameter apertures and corrected to total assuming stellar profiles (aperture corrections of 5% and 20% for the ACS and NICMOS data respectively). Apertures of  $1.8''$  were dropped randomly in empty regions of the IRAC images and then the fluxes corrected to total assuming PSF profiles (aperture correction multiplicative factors of 2.4, 2.7, 3.5, and 3.7 for the  $3.6\mu m$ ,  $4.5\mu m$ ,  $5.8\mu m$ , and  $8.0\mu m$  images re-

By applying the above criteria to  $\sim 80$  arcmin<sup>2</sup> of deep NICMOS data, Bouwens et al. (2009, in preparation) identified 14  $z \sim 7$   $z$ -dropout candidates (see Table 2). The candidates range in  $H_{160,AB}$  magnitude from 25.5 to 27.6 AB mag and are typically only marginally resolved at NICMOS/NIC3 resolution (FWHM of the PSF is  $\sim 0.37''$ ). Contamination rates for the sample are determined by running a number of photometric scattering simulations on a fake sample of low redshift sources. This sample is constructed to match the color distribution of observed galaxies in the  $24.5 < H_{160} < 26$  range. We have added noise to the fluxes in each individual band according to the depths of the different fields. By applying the selection criteria previously described, we characterize when and with what frequency low-redshift contaminants enter our selection. A more detailed discussion of the procedure is given in Bouwens et al. (2008) and Bouwens et al. (2009, in preparation). Through this technique we find that the contamination for the sample (by lower redshift galaxies, time-variable sources, low-mass stars, for example) is expected to be just  $\sim 10\%$  of the sample for sources found over the HUDF and HUDF05 fields, and only  $\sim 20\%$  for sources within the GOODS fields.

We only use those 11  $z$ -dropout candidates from the Bouwens et al. (2009, in preparation) selection that have deep (23+ hr) IRAC data in both  $3.6$  and  $4.5\mu m$  and which were in the Bouwens et al. (2009, in prep)  $z$ -dropout sample as of June 2009.

### 3. OBSERVATIONAL DATA

The very deep optical, near-IR, and mid-IR IRAC data available for our  $z \sim 7$   $z$ -dropout candidates permit us to study the properties of these sources in great detail. A summary of the available imaging data for the candidates we have in our various search fields is given in Table 1.

The deep near-IR data we have available for our candidates at  $\sim 1.1\mu m$  and  $\sim 1.6\mu m$  comes from NICMOS. For the candidates within the GOODS fields, the NICMOS data reach to depths of  $\sim 26.8$  AB mag and  $\sim 26.7$  AB mag ( $5\sigma$ , aperture flux within a  $0.6''$ -diameter, used for detection) in the  $J_{110}$  and  $H_{160}$  bands, respectively. For purposes of the SED fitting we use a larger ( $0.9''$ -diameter) aperture to minimize differences in the aperture corrections among the optical, NIR and mid-IR images. The  $1\sigma$  limits relevant for the SED fitting are  $\sim 27.8$  and  $\sim 27.9$  AB mag ( $J_{110}$  and  $H_{160}$  bands, corrected to total fluxes using aperture corrections of  $\sim 20\%$  derived from stellar profiles). The near-IR data over the HUDF reaches some  $\sim 0.5$  AB mag deeper. The FWHM of the NICMOS PSF is  $0.34''$  and  $0.37''$  in the  $J_{110}$  and  $H_{160}$  bands, respectively.

We also have very deep  $\sim 2.2\mu m$  K-band data available for our  $z \sim 7$   $z$ -dropout candidates over the HUDF and in the central region of the HDF-North. These data are particularly valuable for providing a constraint on the UV-continuum slopes. The K-band data over the HUDF correspond to the 40 hr integration in the best seeing conditions in the  $K_s$ -band filter at ISAAC (VLT) and PANIC (Magellan) (Labbé et al. 2006). We estimate  $1\sigma$  depths of  $\simeq 27.1 - 27.4$  AB magnitudes in  $0.9''$  diameter apertures. The other two sources are in the HDFN and their K-band data come from the deep Subaru GTO MOIRCS imaging campaign (Kajisawa et al.



TABLE 2  
SUMMARY OF PHOTOMETRY.

ID	Field	$B_{435}$	$v_{606}$	$i_{775}$	$z_{850}$	$J_{110}$	$H_{160}$	$K_s^a$	$3.6\mu m$	$4.5\mu m$
UDF-640-1417	HUDF	>29.9	>30.4	>29.9	27.8±0.2	26.5±0.2	26.1±0.2	25.8±0.2	25.2±0.1	25.9±0.4
UDF-983-964	HUDF	>29.9	>30.4	>29.8	>29.2	26.7±0.2	26.8±0.3	26.6±0.6	26.2±0.3	26.6±0.9
UDF-387-1125	HUDF	>30.0	>30.6	>30.0	29.1±0.8	27.7±0.4	26.9±0.3	>27.4	>27.5	>26.8
UDF-3244-4727	HUDF	>30.0	>30.4	>30.0	>29.4	27.6±0.3	26.9±0.3	>27.1	26.5±0.4	26.7±1.0
GNS-zD1	GOODS-S	>28.6	>29.0	>28.3	>27.9	26.5±0.3	26.2±0.2	...	24.9±0.1	25.4±0.4
GNS-zD2	GOODS-S	>28.9	29.0±1.0	>28.4	>28.4	27.0±0.4	26.7±0.3	...	26.4±0.6*	26.2±0.9
GNS-zD3	GOODS-S	>29.1	>29.4	>29.0	>28.7	27.3±0.7	26.7±0.3	...	25.7±0.3	25.9±0.7
GNS-zD4	GOODS-N	>28.5	>28.8	>28.4	>28.4	26.7±0.4	26.3±0.3	...	25.2±0.2	25.4±0.4
GNS-zD5 <sup>b</sup>	GOODS-N	>28.8	>29.1	>28.7	28.1±0.7	26.2±0.3	25.3±0.1	25.4±0.2	24.6±0.1*	25.4±0.3
CDFS-3225-4627	GOODS-S	>28.7	>29.0	>28.6	>28.4	26.8±0.4	26.4±0.3	...	26.1±0.3	26.0±0.5
HDFN-3654-1216 <sup>c</sup>	HDFN	>29.2	>29.4	>28.6	26.5±0.2	26.2±0.2	25.9±0.2	26.4±0.4	25.2±0.3*	25.7±0.7
Mean SED <sup>d</sup>		>30.3	>30.6	>30.1	28.41±0.29	26.70±0.09	26.27±0.07	26.68±0.30	25.58±0.07	25.91±0.18

NOTE. — Magnitudes are total and in the AB system. Optical to near infrared photometry measured in 0.9'' diameter apertures with aperture corrections of 5% - 20% (derived assuming stellar profiles). Mid infrared IRAC photometry performed on "cleaned" images with 1.8'' aperture diameters. Aperture correction factors in this case are 2.4 and 2.7 in the 3.6 and 4.5  $\mu m$  channels respectively. Upper limits and error bars are 1  $\sigma$ .

<sup>a</sup> K-band from either MOIRCS or ISAAC depending on the Field, see Table 1.

<sup>b</sup> MOIRCS  $J_s$  band imaging is deep enough at the location of this source. We measure  $J_s=25.6\pm 0.3$ .

<sup>c</sup> There are additional WFPC2 optical imaging constraints for HDFN-3654-1216:  $B > 30.2$ ,  $V > 29.0$ ,  $i > 28.8$ .

<sup>d</sup> This mean SED was constructed rescaling all the SEDs so that the  $H_{160}$ -band fluxes coincide with the mean value and then averaging all the other bands. The 3.6  $\mu m$  IRAC fluxes from sources GNS-zD2, GNS-zD5, and HDFN-3654-1216 were excluded from the average. See section §6.2 and figure 4.

\* After subtracting a bright nearby neighbor from the 3.6  $\mu m$  image of this source, sizable residuals remain, and so the quoted 3.6  $\mu m$  flux measurements for these sources may suffer from systematic errors.

2006; Ouchi et al. 2007: see Bouwens et al. 2008 for a description of our reductions). We have only made use of the deepest GTO pointing which reaches down to 25.4 total AB magnitudes at  $5\sigma$  (0.9'' diameter apertures). The FWHM for the K-band PSF is  $\sim 0.5''$ .

Deep optical  $B_{435}$ ,  $v_{606}$ ,  $i_{775}$ , and  $z_{850}$  observations are available for our candidates with ACS and typically reach to depths of  $\sim 30$  mag in the HUDF and  $\sim 1.5$  mag shallower in the rest of our fields. For the single  $z$ -dropout candidate in the HDF-North WFPC2 field, we have the very deep ( $\gtrsim 28$  mag at  $5\sigma$ )  $B_{450}$ ,  $V_{606}$ , and  $I_{814}$  WFPC2 observations – which permit us to set very strong constraints on the strength of the Lyman Break.

The Spitzer IRAC imaging data from the GOODS program (Dickinson et al. 2009, in preparation) provide us with deep rest-frame optical coverage on our  $z \sim 7$   $z$ -dropout candidates – which is critical for estimates of the stellar mass in these sources. Two exposures of  $\sim 23$ -hr each were taken in two different epochs with the IRAC camera – rotated by 180 deg – and overlapping in the center of the GOODS field. The region of overlap contains the HUDF in the GOODS South. We find AB magnitude detection limits for point sources of 27.4, 26.6, 25.4, and 25.3 for the 3.6, 4.5, 5.8, and 8.0  $\mu m$  channels respectively (1  $\sigma$ , measured on apertures of 1.8'' in diameter and corrected to total flux assuming stellar profiles with aperture corrections of 2.4, 2.7, 3.5, 3.7 respectively – multiplicative factors). These limiting depths (for single epoch  $\sim 23.3$  hr IRAC observations) were estimated by dropping apertures at random empty regions of the sky and measuring the flux variations. A good summary of the IRAC observations is provided in Labbé et al. (2006) and Stark et al. (2007), for example. In this work we make use of the reductions of Data Release (DR) 3 of epoch 1 observations and DR2 of epoch 2 of the GOODS-

S field. In the case of the GOODS-N field we make use of the reductions of Data Release (DR) 2 of both epochs.

#### 4. PHOTOMETRY

*Optical/near-IR Photometry:* Optical to NIR fluxes were measured in standard 0.9''-diameter circular apertures. We corrected these measured fluxes for the missing light outside these apertures assuming stellar profiles. These latter corrections increased the measured flux by 5% - 20% depending on the band. All the sources in our sample were sufficiently separated from their neighbors that we could use this simple approach, except for the one in the HDFN field where there was a faint but very close (almost overlapping) neighbor. This made it impossible to use the standard circular aperture to measure the flux of HDFN-3654-1216 (ID from Bouwens et al. 2009, in preparation). To ensure our measurement of its flux was not contaminated by the flux of this neighbor, we fitted a PSF profile to the neighbor using GALFIT (Peng et al. 2002) and subtracted it from the image before measuring the flux of this  $z$ -dropout.

*IRAC Photometry:* One of the biggest challenges in estimating the masses of our  $z \sim 7$  candidates is the acquisition of reliable mid-IR fluxes for these candidates from the available IRAC data. The extremely broad PSF of this instrument and large pixel sizes make the images extremely crowded and so fluxes from neighboring sources spill over onto each other. To overcome this issue, a wide variety of different approaches have been developed, almost all of which involve modeling the IRAC image with a number of smoothed sources of varying flux. In the most common cases, the model light profiles are theoretical like the ones produced by GALFIT. The use of these models can result in systematic errors in the photometry if the sources have irregular or clumpy spatial profiles.

We have used here the technique described in

Labbé et al. (2006), which consists in the creation of an empirical light profile based in the higher resolution NICMOS images. This technique uses a segmentation map created by *SExtractor* (Bertin & Arnouts 1996) to define the boundaries of each source in the area to be cleaned (we use a  $2\sigma$  threshold to ensure all the possibly relevant neighbors are fitted) and use the light profiles of the sources within those boundaries as the empirical light profiles (assuming a similarity between the profiles at both  $1.6\ \mu\text{m}$  and  $3.6\ \mu\text{m}$ ). The individual profiles are then convolved with a carefully constructed kernel (based on the instrumental PSFs) to simulate how they would look like in the IRAC images (modulo a normalization factor). Finally we fit for the total flux of each neighbor and subtract them off the image. Instead of using the  $z$ -dropout flux measurement determined from these fits, we subtract off the flux from the neighbors and perform standard aperture photometry in relatively small apertures on the “cleaned” image. We find that the optimal aperture diameter for maximizing the S/N of our flux measurements (assuming point sources) is  $\sim 1.8''$  in all the channels. The aperture corrections are 2.4, 2.7, 3.5, and 3.7 (multiplicative factors) in the 3.6, 4.5, 5.8, and  $8.0\ \mu\text{m}$  channels respectively. The errors in the measured flux include both the typical variations on the sky brightness, and the uncertainty in the flux removed from the aperture.

A simple inspection of our images shows that 5 of the 11  $z \sim 7$   $z$ -dropout candidates in our sample (i.e., GNS-zD2, GNS-zD5, UDF-387-1125, UDF-3244-4727, HDFN-3654-1216) are severely blended with bright foreground sources. The other six sources are somewhat more isolated but with the size of the instrumental PSF it is obvious that flux from neighboring sources will spill over onto these candidates (often contributing  $\gtrsim 20\%$  of the light within the  $1.8''$ -diameter aperture centered on our candidates). From the 5 severely blended sources we are able to satisfactorily “clean” the images in at least 2 cases (we will discuss the other three cases GNS-zD2, GNS-zD5 and HDFN-3654-1216 in the next paragraph). We could check the consistency of the method for 5 of the sources that were imaged in both epochs. As was mentioned before, there is a 180 deg rotation in the IRAC camera (and thus in the asymmetric instrumental PSF) between the two epochs, which makes the light profile models (for the neighboring sources) almost independent. Obtaining consistent fluxes in these two images is a good indication of the reliability of the method. For the sources where IRAC observations are from  $>1$  epoch (and consistent within the measurement errors), we average the fluxes and combine the errors accordingly which reduces them by a factor  $\sqrt{2}$ .

In the cases of GNS-zD2 and GNS-zD5 strong color gradients in the closest neighbor cause the model light profiles to be inadequate and so large residuals are evident (after subtracting the flux from the neighbors). GNS-zD5 was imaged in both epochs and we find a difference of  $2\sigma$  between the measurements in the  $3.6\ \mu\text{m}$  channel but a much cleaner residual (and better agreement) in the  $4.5\ \mu\text{m}$  image. A similar discrepancy was found for the  $3.6\ \mu\text{m}$  flux measurement for HDFN-3654-1216. In this case the poor subtraction is not due to strong color gradients but to the extreme proximity of

its neighbor. In all three cases we adopt the single epoch uncertainty. Given the small size of our present sample of  $z$ -dropouts, we chose to keep these three sources in the sample – keeping in mind the caveat that the flux measurements for these sources could possess large systematic errors. In summary, we are able to perform reliable cleaned photometry on 8 out of the 11 sources (73%).

We obtain  $> 2\sigma$  detections for 9 of the 11 sources in the  $3.6\ \mu\text{m}$  image and for 5 sources in the  $4.5\ \mu\text{m}$  image. The two sources with quite marginal ( $< 2\sigma$ ) detections in both IRAC images are UDF-387-1125 and GNS-zD2. A simple stacking of the images of these two sources (adding both sources in both IRAC images) shows a significant detection, which provides evidence for the reality of the sources.

Optical to mid-Infrared image stamps ( $\sim 4'' \times 4''$ ) for all the sources are presented in figure 1. The  $5.8\ \mu\text{m}$  and  $8.0\ \mu\text{m}$  channels have been omitted because none of the sources are detected in those bands (as expected). The two epochs have been coadded when available. The measured magnitudes are summarized in table 2.

## 5. PHOTOMETRIC REDSHIFTS

Perhaps the most fundamental quantity that we can estimate for galaxies in our  $z_{850}$ -dropout sample is their redshift. We first explore the probable redshifts of our sources using the photometric redshift code EAZY (Brammer et al. 2008). The code works by comparing the observed photometry with that predicted on the basis of the specific SED templates. We use the default template set, which was derived from the Pegase population synthesis models (Fioc & Rocca-Volmerange 1997) and optimized to reproduce the properties of galaxies in the range  $0 < z < 4$ . Comparisons of the photometric redshift estimates output from EAZY with some of the deepest spectroscopic surveys available show minimal systematic errors and a scatter in  $z_{\text{spec}} - z_{\text{phot}}$  of  $\sigma = 0.034$  over the range  $0 < z < 4$  (see table 1 in Brammer et al. 2008). The few sources at higher redshifts ( $z \sim 6$ ) with available spectroscopy are also in good agreement with its photometric redshift estimates. One relevant advantage over other photometric redshift codes is that EAZY works with fluxes instead of magnitudes and naturally handles negative measurements which are common in our optical bands.

We use the available flux measurements in the  $B_{435}$ ,  $V_{606}$ ,  $i_{775}$ ,  $z_{850}$ ,  $J_{110}$ ,  $H_{160}$ ,  $3.6\ \mu\text{m}$ ,  $4.5\ \mu\text{m}$  bands, and also the  $B_{450}$ ,  $V_{606}$ ,  $I_{814}$ ,  $K$  bands if available for our photometric redshift estimates. We do not include the IRAC  $5.8\ \mu\text{m}$  and  $8.0\ \mu\text{m}$  flux measurements of the sources (consistent with no detection) in the comparison – since they do not help us to meaningfully discriminate between the competing redshift solutions. We restrict the redshift range of our fits to  $z \sim 4 - 11$  and adopt no redshift prior. Solutions at  $z \sim 1.5$  are also possible for most of the sources but at lower probability for all of them. However, quantifying this is challenging given our poor knowledge of the demographics of galaxies at both  $z \sim 1.5$  and  $z \sim 7$ . Furthermore, the existence of synthetic solutions at any of these redshifts does not necessarily imply the existence of real galaxies with the observed properties. We have provided an independent (short) description of the estimate of the fraction of low-redshift contaminants in §2. A more detailed discus-

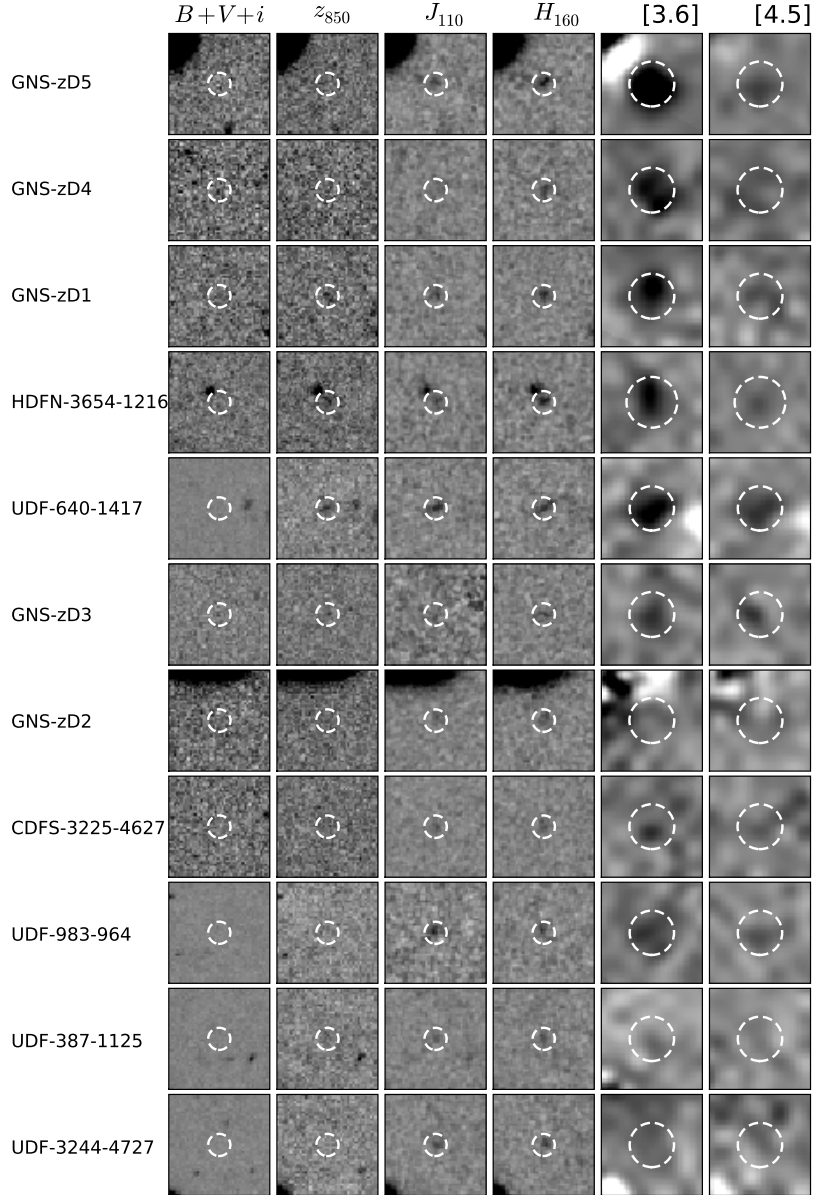


FIG. 1.— Postage stamps of the  $z_{850}$ -dropouts. Each stamp is  $4'' \times 4''$  in size ( $\sim 21$  kpc at  $z = 7$ ). The dashed circles indicate the apertures used for photometry ( $0.9''$  for the optical to NIR and  $1.8''$  in the IRAC bands). All the sources are undetected in  $B_{435}$ ,  $v_{606}$ , and  $i_{775}$  and only UDF-640-1417 and HDFN-3654-1216 are weakly detected in  $z_{850}$ . The latest two sources are estimated to be the lowest redshifts of the sample.  $3.6 \mu\text{m}$  and  $4.5 \mu\text{m}$  stamps show the sources after the flux from the nearby neighbors have been fit and removed (i.e., they are “cleaned” images), with the two epochs of IRAC data added together when available. The cleaning process in the case of sources GNS-zD5 and GNS-zD2 has left nearby residuals (seen in white) attributed to the close and bright nearby sources visible in the other bands. To a lesser degree this seems to also be the case for sources UDF-640-1417 and UDF-3244-4727. Since these latter sources were observed in both epochs, it was possible to check that the measured fluxes are consistent among them. As expected, all sources are undetected in the  $5.8$  and  $8.0 \mu\text{m}$  channels. The sources have been placed in order of increasing  $H_{160}$  magnitude from top to bottom.

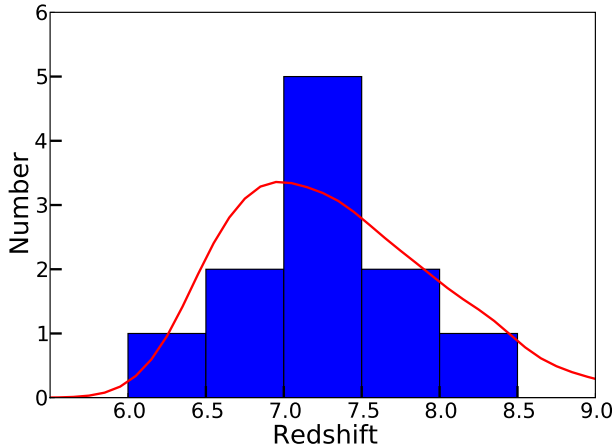


FIG. 2.— The photometric redshifts of our  $z \sim 7$   $z$ -dropout sample (histogram). The solid line shows the redshift distribution that Bouwens et al. (2008) predict for the  $z$ -dropout selection. The photometric redshifts were estimated with EAZY (see §4). Typical uncertainties in the redshift for individual sources is  $\Delta z \sim 0.6$ . The lowest redshift in the sample corresponds to object HDFN-3654-1216 at  $z = 6.2$ . This object presents the bluest  $z_{850} - J_{110}$  color due to it being weakly detected in the  $z_{850}$  band image.

sion is provided in the Bouwens et al. (2009, in preparation) study where the sample is described (but see also Bouwens et al. 2008 which describes the estimate for a similar sample). The estimated contamination fraction for this sample is  $\sim 10\%$  and  $\sim 20\%$  for sources in the HUDF and outside the HUDF, respectively.

We explore the solutions in the range  $4 < z < 11$  in a grid with steps of 0.01. At each step there is a  $\chi^2(z)$  value associated with the best solution that is used to create a probability function  $p(z) \propto \exp[-\chi^2(z)/2]$ . The redshift is estimated marginalizing over this probability and probability contours are used to determine the 68% confidence intervals. Because of the shape of this function at redshifts  $z > 7$ , the estimated redshifts are usually located somewhat above the absolute minimum  $\chi^2$ . The typical uncertainties we estimate for individual sources are in the order of 0.6. Finally, the redshift distribution obtained from EAZY is  $z = 7.2 \pm 0.5$ , similar to what would be expected based on the shape of the ACS  $z_{850}$  passband and the color cuts imposed in the sample (see figure 2).

## 6. STELLAR POPULATION MODELING

We can make sense of the present photometric selection of  $z$ -dropouts in terms of their *intrinsic* properties – like age, stellar mass, or dust extinction – by modeling the spectral energy distributions observed for individual sources. Such modeling is now ubiquitous in the literature (Sawicki & Yee 1998; Brinchmann & Ellis 2000; Papovich et al. 2001; Labbé et al. 2007), and has proven quite powerful in the interpretation of distant galaxies – both given the abundance (and quality) of photometric data and the plausibility of the photometric estimates. Indeed, studies have found reasonable agreement between stellar masses determined from such modeling and those determined from the dynamics (Erb et al. 2006).

Here we model the stellar populations with the

Bruzual & Charlot (2003) (BC03) spectral synthesis libraries. Over the wavelength range covered by the present study, these libraries show almost no difference with respect to the newest Charlot & Bruzual (2007) (CB07, e.g. Stark et al. 2009; Labbé et al. 2010) and have been shown to be in reasonable agreement with other libraries (e.g., Maraston 2005). We use a Salpeter (1955) Initial Mass Function (IMF) between 0.1 and 100  $M_{\odot}$  and sub-solar metallicity ( $0.2 Z_{\odot}$ ) so that comparisons to existing works are more straightforward. Our selection of sub-solar metallicity models is based on the observed trends at high redshifts (e.g. Maiolino et al. 2008) as well as on the direct observations of extremely blue UV slopes of the most recently found  $z \sim 7$  sources (Bouwens et al. 2010b, Labbé et al. 2010). However, since other IMFs (or metallicity models) fit our observations just as well, we will remark on how the results change if we adopt a different IMF or metallicity. For simplicity, we assume a constant star formation (CSF) rate when modeling the star formation histories of the galaxies in our sample. This assumption seems preferable to an exponentially-decaying SF history (which implies increasing SFRs with redshift), as there is currently no evidence that UV-selected samples form stars at a faster rate at earlier epochs (e.g., Papovich et al. 2001, Stark et al. 2009, and others).

Finally, given the challenges in constraining both age and reddening based upon the photometric information available for individual sources, we will assume that galaxies in our sample show negligible dust extinction when doing the stellar population modeling. We have good reasons for making this assumption.  $z \gtrsim 5$  galaxies have been found to have very blue  $UV$ -continuum slopes  $\beta$  and thus little dust extinction (e.g., Lehnert & Bremer 2003; Stanway et al. 2005; Yan et al. 2005; Bouwens et al. 2006, 2009a). As we will show later, a similarly steep  $UV$ -continuum slope  $\beta$  ( $-2.4 \pm 0.4$ ) is found for the mean SED of our sample (§6.2) – again suggesting minimal dust extinction. For individual sources, however, it is difficult for us to obtain useful constraints on the  $UV$ -continuum slope and hence dust extinction. While we have high quality  $H_{160}$ -band fluxes for our candidates, the other fluxes we have which probe the  $UV$ -continuum are not adequate: the  $J_{110}$ -band fluxes we have available depend significantly on the redshift of the source (the  $J_{110}$ -band extends to  $\sim 8000 \text{ \AA}$ ) and the  $K$ -band fluxes (available on fewer sources) are more uncertain in general (due to the shallower nature of the  $K$ -band imaging data). We have tested the impact of allowing modest amounts of extinction ( $A_V < 0.5$ ) to the models and found that the main results (SMD, SSFR, ages) are unchanged or at least consistent within the uncertainties.

Within these general specifications, we explored a wide variety of different parameters (redshift, Age) in modeling the observed photometry of each  $z \sim 7$  candidate:

$$z = 4.0 - 11.0 \text{ (steps of 0.01)}$$

$$\log(\text{Age}[\text{Myr}]) = 7.5 - \text{Age}_{max} \text{ (steps of 0.01)}$$

where  $\text{Age}_{max}$  is the age of the universe at the corresponding redshift so that the models avoid solutions in which the populations are older than the universe.



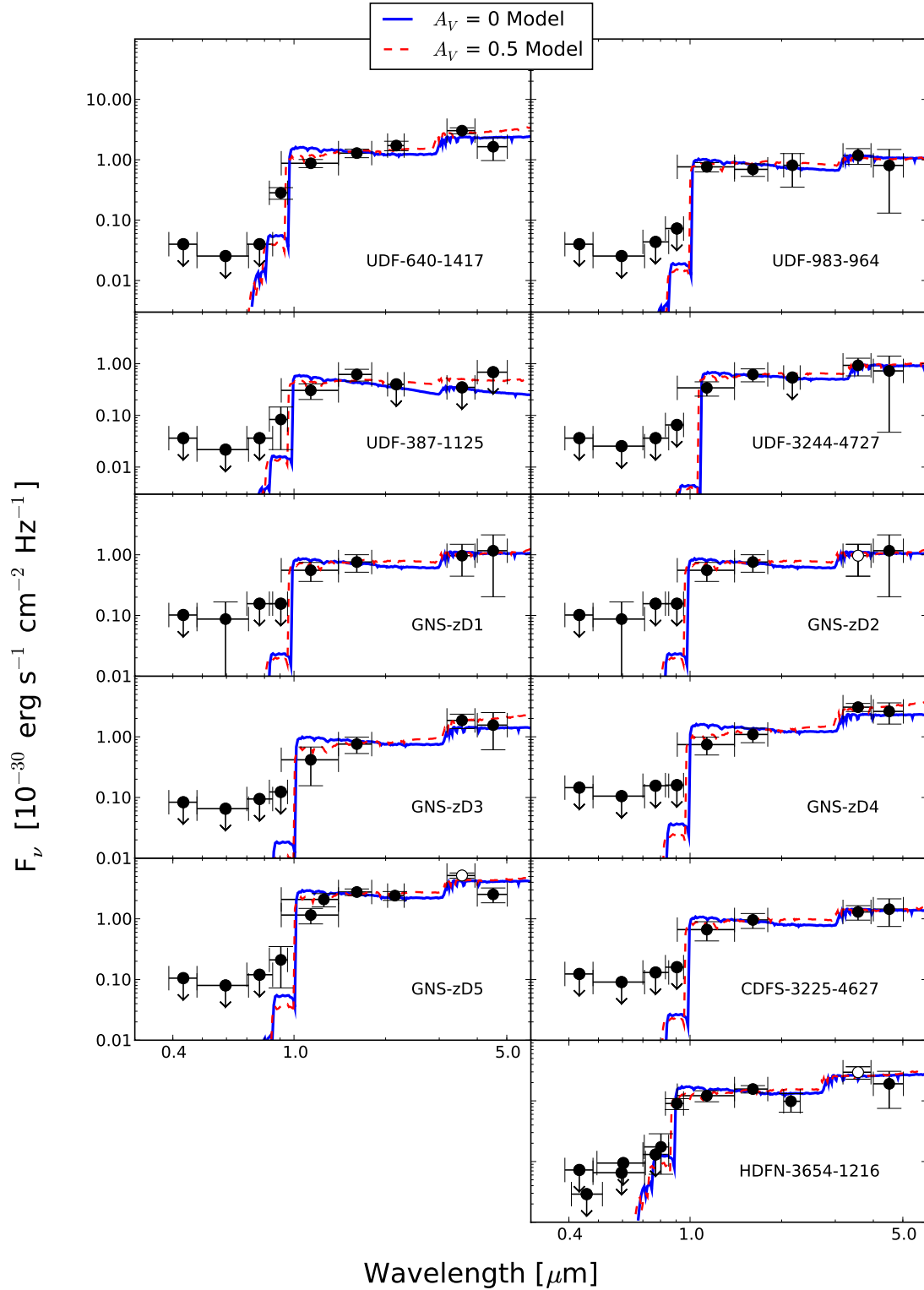


FIG. 3.— Observed SEDs and synthetic stellar population model fits. The error bars and upper limits are  $1\sigma$ . The models shown here are from Bruzual & Charlot (2003) with a Salpeter IMF and  $0.2 Z_{\odot}$ . The red curve represents the best fit models without extinction and the blue curve shows the effect of imposing a maximal extinction of  $A_V = 0.5$ . The open circles shown for the  $3.6 \mu\text{m}$  flux measurements of objects GNS-zD2, GNS-zD5, and HDFN-3654-1216 correspond to points with poor photometry.



TABLE 3  
SUMMARY OF BC03 MODELS FIT PARAMETERS. 0.2  $Z_{\odot}$ , SALPETER IMF, CONSTANT SFR,  $A_V = 0$ .

ID	$z_{phot}$	Mass [ $10^9 M_{\odot}$ ]	Age $_w$ <sup>a</sup> [Myr]	SFR $_{L_{1500}}$ [ $M_{\odot} yr^{-1}$ ]	SFR [ $M_{\odot} yr^{-1}$ ]	SSFR <sup>b</sup> [ $Gyr^{-1}$ ]	$L_{UV}$ [ $10^{10} L_{\odot}$ ]	U-V	$H_{160} - 3.6$	$\chi^2_{red}$
UDF-640-1417	$6.9^{+0.1}_{-0.1}$	$6.6^{+0.3}_{-0.9}$	379	13.2	$10.5^{+0.7}_{-0.7}$	$2.0^{+0.3}_{-0.1}$	5.4	0.5	0.9	1.7
UDF-983-964	$7.3^{+0.4}_{-0.3}$	$2.2^{+2.0}_{-1.5}$	173	9.0	$7.4^{+2.4}_{-1.4}$	$4.1^{+8.9}_{-1.9}$	3.7	0.1	0.6	0.4
UDF-387-1125	$7.1^{+2.0}_{-0.5}$	$0.2^{+1.4}_{-0.1}$	19	4.8	$5.2^{+5.0}_{-2.4}$	$25.6^{+12.3}_{-22.6}$	2.0	-0.7	-0.8	0.3
UDF-3244-4727	$7.9^{+0.8}_{-0.6}$	$2.8^{+0.5}_{-2.1}$	315	6.8	$5.4^{+2.0}_{-1.2}$	$2.4^{+6.9}_{-0.4}$	2.8	0.4	0.4	0.9
GNS-zD1	$7.2^{+0.2}_{-0.2}$	$7.6^{+0.4}_{-0.5}$	362	15.8	$12.6^{+1.2}_{-1.1}$	$2.1^{+0.1}_{-0.1}$	6.5	0.5	1.3	1.5
GNS-zD2	$7.1^{+1.5}_{-0.6}$	$2.5^{+1.8}_{-2.2}$	251	7.3	$5.9^{+6.4}_{-1.6}$	$3.0^{+24.7}_{-1.3}$	3.0	0.3	0.3	0.4
GNS-zD3	$7.3^{+0.9}_{-0.4}$	$4.2^{+0.4}_{-1.5}$	354	8.8	$7.1^{+2.0}_{-1.1}$	$2.1^{+1.2}_{-0.2}$	3.6	0.4	1.0	0.3
GNS-zD4	$7.2^{+0.4}_{-0.2}$	$6.8^{+0.3}_{-0.7}$	362	13.9	$11.2^{+1.4}_{-1.2}$	$2.1^{+0.3}_{-0.1}$	5.7	0.5	1.1	0.8
GNS-zD5	$7.3^{+0.2}_{-0.2}$	$12.3^{+0.3}_{-2.1}$	354	26.1	$20.9^{+1.5}_{-1.4}$	$2.1^{+0.4}_{-0.0}$	10.7	0.4	0.7	2.3
CDFS-3225-4627	$7.1^{+1.5}_{-0.5}$	$3.5^{+2.0}_{-2.3}$	281	9.2	$7.4^{+5.2}_{-1.8}$	$2.7^{+5.2}_{-1.0}$	3.8	0.3	0.3	0.6
HDFN-3654-1216	$6.3^{+0.2}_{-0.2}$	$6.9^{+0.3}_{-3.8}$	426	12.4	$9.8^{+1.7}_{-0.9}$	$1.8^{+2.2}_{-0.1}$	5.1	0.5	0.7	0.8
Mean SED <sup>c</sup>	$7.3^{+0.1}_{-0.0}$	$6.3^{+0.1}_{-0.1}$	354	13.4	$10.7^{+0.5}_{-0.2}$	$2.1^{+0.0}_{-0.0}$	5.5	0.4	0.7	3.3

NOTE. — Best fit parameters, 68% confidence intervals and corresponding  $\chi^2$  for Bruzual & Charlot (2003) fits with subsolar metallicity (0.2 $Z_{\odot}$ ) and Salpeter IMF between 0.1 and 100  $M_{\odot}$ . We obtain a redshift for the sample of  $7.2 \pm 0.5$ . The models suggest that in some of these galaxies most of the stars were born at considerably earlier times ( $z \lesssim 10$ ), well into the epoch of reionization. The masses of these sources range 0.2-12 $\times 10^9 M_{\odot}$ . We have restricted the dust extinction to zero, consistent with the trend observed at these high redshifts. SFRs from the models are consistent with the ones derived from the extrapolated  $L_{1500}$  using the usual Madau et al. 1998 formula. These SFRs are somewhat high,  $\sim 10 M_{\odot} yr^{-1}$  typically. The mean SSFRs of the sample is  $2.4 \pm 0.6 Gyr^{-1}$ , with an outlier corresponding to the youngest model. The estimated best fit ages do not change considerably if we consider either Chabrier IMF or solar metallicity models. As expected for a Chabrier IMF, the masses derived are a factor  $\sim 0.55$  lower and so are the SFRs. Solar metallicity models produce masses  $\sim 10\%$  larger. The maximal extinction model with  $A_V = 0.5$  produces  $\sim 45\%$  lower ages and  $\sim 45\%$  higher masses (with the consequent increase in SFR) with more scatter.

<sup>a</sup> Age $_w$  corresponds to the SFH-weighted ages. In the case of CSF models, this simply corresponds to half the time since the onset of star formation. The typical uncertainties in this quantity are substantial ( $^{+70}_{-120}$  Myr).

<sup>b</sup> The SSFR (= SFR/Mass) here is derived from the extrapolated  $L_{1500}$  luminosity and the masses from the CSF models.

<sup>c</sup> These are not the mean values of the best fit parameters derived for the sample but rather the parameters derived from the modeling of the mean SED described in §6.2 (see figure 4).

To derive 68%, 95%, and 98% confidence intervals for the above parameters, we ran a number of simulations where we added photometric scatter (noise) to the observed fluxes and then used the results to determine the threshold  $\chi^2$  values that encompass these confidence intervals. We performed the above calculations with the stellar population modeling code named FAST (see appendix in Kriek et al. 2009).

Note that in stellar population modeling, we do not use the photometric redshift estimates from the previous section. This was to avoid additional complications in the definition of the confidence intervals (as the templates are slightly different). However, we found that the two redshift estimates are consistent (the typical discrepancies are rms  $\Delta z \sim 0.04$ ).

In figure 3, the observed SEDs are presented along with the best fit models with no extinction. The corresponding properties we derive for these galaxies using these models are detailed in table 3. The ages in that table correspond to the average age of the stellar population, i.e.,  $M_{\text{total}}^{-1} \int t_{\text{lookback}} \text{SFR}(t_{\text{lookback}}) dt_{\text{lookback}}$  ( $=\text{age}_w$ ). In the case of constant SFR models, this is simply equal to one half of the time elapsed since the onset of star formation. Similar to what others have found at somewhat lower redshifts, these models indicate the presence of quite massive systems very early in the universe. We find masses in the range of  $0.2 - 12 \times 10^9 M_{\odot}$ . These models also show quite large ages that place the formation of most of the stars up to 380 Myrs earlier with typical values in the order of 300 Myr. The uncertainties in the derived age, however, are quite substantial, typically  ${}_{-120}^{+70}$  Myr (68% confidence intervals). From table 3, it can be noticed that the values of  $\text{age}_w$  imply that some galaxies have been forming stars for times comparable to the age of the Universe at this redshift. We have preferred not to impose any arbitrary restrictions on the time of onset of star formation because any meaningful redshift constraint (e.g.  $z < 100$ ) would not meaningfully restrict the ages (16 Myr for  $z < 100$ ), particularly when compared to the uncertainties associated with the estimation, typically  ${}_{-120}^{+70}$  Myr. Such constraint implies insignificant fractions of stellar mass assembled at extreme redshifts.

### 6.1. Parameter dependencies

In the above stellar population modeling, we adopted a Salpeter IMF and assumed sub-solar metallicity ( $0.2Z_{\odot}$ ). We also explored the effects of using a Chabrier IMF and of varying the metallicity of the models. We find that while distribution of best fit redshifts and ages is unchanged, the derived masses are  $\sim 45\%$  smaller if we use Chabrier IMF (instead of Salpeter), and 10% larger if we consider models with solar metallicity (instead of  $0.2Z_{\odot}$ ). For both metallicities ( $0.2Z_{\odot}$  and  $Z_{\odot}$ ) and both IMFs (Chabrier and Salpeter), we obtain reasonable  $\chi^2$  fit results, so there is no reason to prefer one IMF or metallicity over the others.

We have also assumed that our sources suffer from minimal dust extinction (both due to the very blue  $UV$ -continuum slope  $\beta$  measured from the mean SED here [§6.3] and due to the blue  $UV$ -continuum slopes  $\beta$  observed at  $z \gtrsim 5$ : Lehnert & Bremer 2003; Stanway et al. 2005; Yan et al. 2005; Bouwens et al. 2006, 2009a). How-

ever, this extinction is not very well constrained for individual  $z \sim 7$  galaxies (which lack strong constraints on their  $UV$ -continuum slopes), and so it is worthwhile to mention how larger values of the dust extinction would affect the ages and stellar masses derived from our modeling. Imposing an extinction of  $A_V = 0.5$  (following Calzetti et al. 2000 – we consider this a safe upper limit based on the previously mentioned studies), yields best fit models that are  $\sim 40\%$  more massive (to compensate for the dimming) but  $\sim 45\%$  younger (which prevents their  $H - [3.6]$  colors from becoming too red to match the observations) with the consequent increase in SFR. We also find reasonable  $\chi^2$  for these models.

Finally, we must remember that we adopted a specific form for the star-formation history – supposing the SFR for each was constant in time. We could easily have adopted other star formation histories (instantaneous burst, exponentially decaying) in fitting the observed SEDs and found acceptable results. To determine the approximate effect of the star formation history on our derived parameters, we also considered exponentially decaying  $e^{-t/\tau}$  histories and instantaneous bursts in modeling our sources. In general we found larger ages and masses for histories with larger  $\tau$ 's (where  $\tau$  for a constant SFR model is of course  $\infty$  and 0 for an instantaneous burst) though all assumed histories produced acceptable fits. In that sense, the unrealistic instantaneous burst models provide a lower limit for the  $\text{age}_w$  of the sample that we find to be 80 Myr. Using a more reasonable approximation like  $\tau = 100$  Myr this number goes up to 170 Myr. This latest result would imply that we are observing a quiescent population right after the main star formation episode is over, which seems unlikely.

While we note these dependencies, we will use our fit results assuming no dust extinction, a Salpeter IMF, sub-solar metallicity ( $0.2Z_{\odot}$ ), and a constant SFR when deriving results in subsequent sections and in particular to estimate the Stellar Mass Density (SMD) of the universe. Relaxing our assumption that there is no dust extinction ( $A_V=0$ ) to  $A_V < 0.5$  produces no significant change in the derived quantities.

### 6.2. Average Spectral Energy Distribution

One significant challenge in modeling the stellar populations of  $z$ -dropouts in our sample is the faintness of the sources and therefore the still sizeable uncertainties on the fluxes we derive. Consequently, it becomes difficult for us to obtain tight constraints on the model parameters – like dust or age – for individual sources.

We can obtain much tighter constraints on the properties of our  $z \sim 7$  galaxy candidates by averaging the measured fluxes for the sources and deriving a mean spectral energy distribution, per unit wavelength. This is particularly valuable for a determination of the  $UV$ -continuum slope  $\beta$  for the sample, since this slope is constrained from the  $H$  and  $K_s$ -band fluxes and since the  $K$ -band flux is only poorly constrained for individual sources. To derive this mean SED, we first normalize all the sources to the average  $H_{160}$ -band flux and then take a weighted mean of the fluxes of all sources ( $\langle x \rangle = \sum(x_i/\sigma_i^2)/(\sum 1/\sigma_i^2)$ ). The mean  $K$ -band flux is derived from the 6 sources where we have deep  $K$ -band data. The sources with poor photometry (GNS-

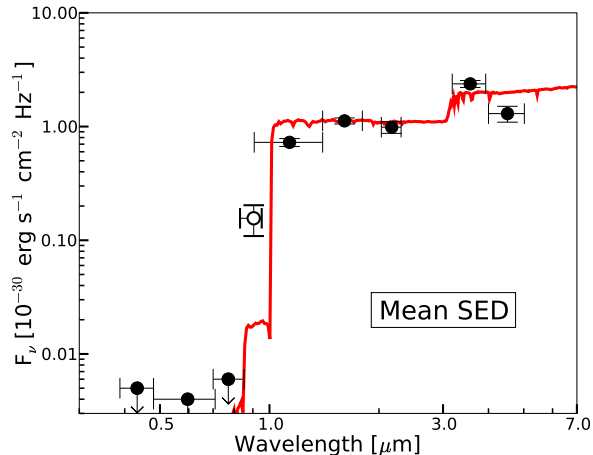


FIG. 4.— The average observed SED (black circles) for galaxies derived from the 11 sources in our  $z$ -dropout selection. Error bars and upper limits are at  $1\sigma$ . The fluxes of each source in our  $z \sim 7$   $z$ -dropout selection was scaled so that their  $H_{160}$ -band flux matched the average  $H_{160}$ -band flux for the sample, after which the rescaled fluxes from the entire sample were averaged. Flux measurements which were poor (due to difficulties in precisely subtracting a nearby neighbor, as for the  $3.6\mu\text{m}$  flux measurements of GNS-zD2, GNS-zD5, and HDFN-3654-1216) were not included in the average. Note, the average  $K$ -band flux we derive here was only determined from the 6 sources for which we had deep  $K$ -band data. Stellar population models were fit to this average observed SED using the same technique that what was used for individual sources (model shown in solid line). The parameters of the fit are presented in table 3. The average  $z_{850}$ -band flux (open circle) was not included in the fit – since it would not make sense to include both the  $z_{850}$  and  $J_{110}$ -band flux (both of which have a different dependence on redshift) in the fits. This average SED shows no detection in the optical  $B$ ,  $V$ , or  $i$  bands and a very large break ( $>3$  mag) between the optical and  $J$  bands – suggesting that the majority of sources in our sample do in fact correspond to  $z \sim 7$  galaxies. The extremely blue  $H - K$  color, which traces the UV continuum, imply that the dust reddening must be very low – consistent with our assumptions in modeling individual  $z$ -dropouts (§6). The pronounced break ( $\sim 1$  mag) between the  $K$  and the  $3.6\mu\text{m}$  bands suggests the presence of a Balmer break, indicating that the typical  $z \sim 7$  galaxy has experienced several previous generations of star formation. We have used the derived  $M/L$  ratio from this mean SED to make a simplified estimate of the stellar mass density of the universe at  $z \sim 7$  of  $4.5 \times 10^5 M_{\odot} \text{Mpc}^{-3}$  (see §7).

$z$ D2, GNS- $z$ D5 and HDFN-3654-1216 in  $3.6\mu\text{m}$ ) were not considered when taking the mean. The mean SED is presented in Table 2 and Figure 3. The  $UV$ -continuum slope  $\beta$  we estimate from the  $H$  and  $K$  photometry is  $-2.4 \pm 0.4$ .

We perform the stellar population modeling for this source in the same way as for the other sources and include the estimated properties in Table 3. When modeling, however, the  $z_{850}$  flux has not been included in the fits to minimize the influence of our lowest redshift sources. The best-fit model is also compared with the mean SED in Figure 3. If we allow the dust reddening to be non-zero and include that in the fits, we find a best fit  $A_V = 0.4$ . This provides support for our assumption in §6 that our  $z \sim 7$  galaxy candidates are largely dust free. Using the mass of the best fit to the mean SED ( $6.3 \times 10^9 M_{\odot}$ ) and the extrapolated luminosity at  $1500 \text{ \AA}$  ( $5.5 \times 10^{10} L_{\odot}$ ) we infer a mass to light ratio of  $M/L_{UV} = 0.12 M_{\odot}/L_{\odot}$ , and also a  $M/L_V = 0.28 M_{\odot}/L_{\odot}$  (from  $L_V = 2.2 \times 10^{10} M_{\odot}$  measured from the best fit model at  $5500 \text{ \AA}$ ). We will use these  $M/L$  ratios to provide one

estimate of the stellar mass density in §7.

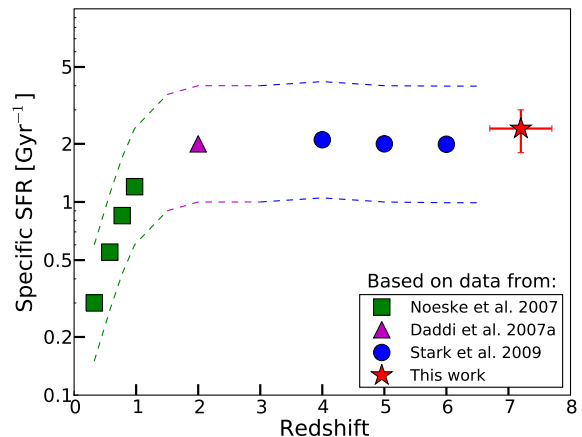


FIG. 5.— The SSFR measured from our data at  $z \sim 7$  compared to the values derived from the data presented by others at a constant stellar mass of  $5 \times 10^9 M_{\odot}$  (corresponding to the median of the present sample). Our estimates of the SSFR are based on results from Noeske et al. (2007), Daddi et al. (2007) (in good agreement with Papovich et al. 2001), and Stark et al. (2009). We estimate that the typical errors at  $z < 7$  (dashed lines) are  $\sim 0.3$  dex. The SSFR seems to be remarkably constant at  $2 \text{ Gyr}^{-1}$  between  $z \sim 2 - 7$  suggesting that the star formation - mass relation does not evolve strongly between  $z \sim 2 - 7$ . The drop observed at  $z < 2$ , however, indicates that some physical process might be inhibiting star formation. This result suggests that star formation in galaxies at  $z \gtrsim 2$  follows somewhat different principles than for galaxies at  $z \lesssim 2$ .

### 6.3. Specific Star Formation Rate

A key quantity in considering the build-up of stars within a galaxy is the specific star formation rate – similar to the  $b$  parameter which was more frequently used in the past to characterize a galaxy’s star-formation history. It is the star formation rate within a galaxy divided by its stellar mass – or equivalently the fraction of the stellar mass in a galaxy that forms per unit time. As such, the SSFR provides us with a useful way of thinking about galaxy growth over cosmic time – and so it is not surprising that it has been estimated out to  $z \sim 6$ .

Here we make use of our best fit synthetic models to estimate  $L_{1500}$  and then use the usual formula from Madau et al. (1998) to estimate the SFR. We combine this with the masses of the best fit models to obtain the specific SFR (see caption in table 3). We find values of  $1.8 - 4.1 \text{ Gyr}^{-1}$  for this quantity across our sample, with a median value of  $2.4 \pm 0.6 \text{ Gyr}^{-1}$  (the outlier at  $\sim 20 \text{ Gyr}^{-1}$  is undetected in the mid-IR so the constraints are poor). To put this value in context, it makes sense for us to compare our derived SSFRs with the values at lower redshift. Given that the SSFRs can depend somewhat on stellar mass, we compare our results to the same median mass as we find in our sample,  $5 \times 10^9 M_{\odot}$ . From the data presented in Stark et al. (2009), we find  $2.1, 2.0,$  and  $2.0 \text{ Gyr}^{-1}$  in their  $z \sim 4, 5,$  and  $6$  samples; from Papovich et al. (2001), Sawicki et al. (2007) and Daddi et al. (2007) we find  $\sim 2 \text{ Gyr}^{-1}$  at  $z \sim 2$ ; and from Noeske et al. (2007) we estimate  $0.3 - 1.2 \text{ Gyr}^{-1}$  for  $z \sim 0.2 - 1$  samples. At  $z \sim 2$ , Reddy et al. (2006)

find a much higher value of  $\sim 10 \text{ Gyr}^{-1}$  but at that mass it is only based on MIPS detected sources. Obviously, any MIPS-detected sample would be biased to include only those sources with substantial enough SFR to show MIPS detections, and hence probably is not representative for the  $10^{9.5} M_{\odot}$  population. The results are shown in Figure 5.

From  $z \sim 7$  to  $z \sim 2$ , there is little apparent evolution in the SSFR and the present results provide a continuation of the trend delineated by Stark et al. (2007) and Yan et al. (2006) from the Reddy et al. (2006) points. However, from  $z \sim 2$  to  $z \sim 0$  the SSFR shows a rapid decrease. This suggests that SFR at  $z > 2$  mostly proceeds in a largely similar way, but that at  $z < 2$  there must be some physical processes inhibiting SFR. Similar to many other comparisons of merit, e.g., evolution of  $M^*$  with redshift (Bouwens et al. 2006; Yoshida et al. 2006; Bouwens et al. 2007), we find that SF in galaxies at  $z \gtrsim 2$  seems to follow somewhat different principles than for galaxies at  $z \lesssim 2$ .

## 7. STELLAR MASS DENSITY

One of the most fundamental quantities we can try to infer from  $z \sim 7$  selections and the present stellar population modeling is the stellar mass density. The stellar mass density tells us how much star formation occurred in the universe to the point of observation, and therefore provides us with a very powerful constraint on early galaxy formation.

### 7.1. Selection Volumes

An essential step in determining the stellar mass density from our  $z \sim 7$   $z$ -dropout selection is obtaining an accurate estimate of the selection volume. This requires that we model the selection of dropout galaxies from all six of the Bouwens et al. (2009, in preparation) search fields and estimate the effective volume we are able to search versus  $H_{160}$ -band magnitude. The selection volumes are calculated by adding artificial sources to our search fields and then attempting to reselect them as  $z \sim 7$   $z$ -dropouts according to the criterion described in §2. The artificial sources are assumed to have a mean  $UV$ -continuum slope  $\beta$  of  $-2$ , consistent with the observed trends a  $4 < z < 6$  (Bouwens et al. 2009a). Their pixel-by-pixel surface brightness profiles are identical to those of random  $z \sim 4$   $B$ -dropouts from the HUDF (Bouwens et al. 2007) of similar brightness but their sizes have been rescaled as  $(1+z)^{-1}$ , following the observed size trends with redshift at  $z > 2$  (Oesch et al. 2009d; Ferguson et al. 2004; Bouwens et al. 2004b). We have not included the possible contribution from Lyman alpha emission to the SEDs. A more detailed description of these simulations can be found in Bouwens et al. (2009, in preparation: but see also Bouwens et al. 2008).

We estimate the following total search volumes as a function of  $H_{160}$ -band magnitude for the entire Bouwens et al. (2009, in preparation)  $z \sim 7$   $z$ -dropout selection (from both the HST NICMOS and ground-based near-IR data):

$$V_{eff}(H_{160}) = \begin{cases} 33 \times 10^4 \text{ Mpc}^3, & \text{if } 25.3 < H_{160} < 25.8 \\ 16 \times 10^4 \text{ Mpc}^3, & \text{if } 25.8 < H_{160} < 26.3 \\ 6.0 \times 10^4 \text{ Mpc}^3, & \text{if } 26.3 < H_{160} < 27.1 \\ 1.2 \times 10^4 \text{ Mpc}^3, & \text{if } 27.1 < H_{160} < 27.5 \end{cases}$$

### 7.2. Stellar Mass Density Determinations

We proceed now to estimate the stellar mass density of the sources we find in these search volumes. We do so in the three different ways we detail below:

*Direct Approach:* Here we estimate the stellar mass density by simply summing over the expected mass density to come from each source. The expected mass density is simply the estimated stellar mass for a source multiplied by the the likelihood it is not a contaminant (90% for sources in the HUDF and 80% otherwise) divided by the selection volume above. The stellar mass density we derive by summing over the 11 sources is  $5.7 \times 10^5 M_{\odot} \text{ Mpc}^{-3}$ . We estimate the uncertainties in the mass density by bootstrap resampling (detailed below). This approach has the advantage of being very direct and even-handedly including all candidates in our selection in the estimate. The disadvantage, of course, is that this estimate may be affected by the mass estimates of the three  $z$ -dropouts with perhaps unreliable  $3.6 \mu\text{m}$  fluxes.

*Mean SED Approach:* For our second estimate, we use our average SED from §6.2 to derive the mean  $M/L_{UV}$  ratio for sources in our sample – reasoning that this  $M/L$  ratio is much more accurately known than any individual  $M/L$  ratio in our sample. For our second estimate, we use our average SED from §6.2 to derive the mean  $M/L_{UV}$  ratio for sources in our sample – reasoning that this  $M/L$  ratio is much more accurately known than any individual  $M/L$  ratio in our sample. If the photometric redshifts are accurate ( $z \sim 7.2 \pm 0.5$ ), then the limiting depth of our search corresponds to  $\sim M_{UV,AB} = -20$ . We have then used the Bouwens et al. (2008)  $UV$  LF at  $z \sim 7$  to estimate the  $UV$  Luminosity density integrated to that depth and multiplied it by the  $M/L_{UV}$  ratio to obtain a stellar mass density of  $4.5 \times 10^5 M_{\odot} \text{ Mpc}^{-3}$ . Again for the uncertainties, we rely on a bootstrap resampling procedure (below).

*Random M/L Approach:* For our final estimate of the stellar mass density, we ran a monte-carlo simulation where we match up the 11 galaxies in our  $z \sim 7$   $z$ -dropout sample with randomly sampled  $M/L$  ratios from the 8 galaxies with reliable IRAC fluxes. We then divide the masses by the search volumes that correspond to their  $UV$  luminosities. After repeating the match up process 100000 times we find a median value of  $6.6 \times 10^5 M_{\odot} \text{ Mpc}^{-3}$ . The estimate of the uncertainties based on bootstrap resampling is described below.

*Uncertainty Estimates:* To estimate the uncertainties in our estimate of the stellar mass density at  $z \sim 7$ , we must fold in the many uncertainties that contribute to this density, including uncertainties in the sampling of the LF, the  $M/L$  ratios of the galaxies we uncover in our search, whether any individual source is a contaminant, and finally the mass estimates themselves of candidates in our sample.

The simplest way of including all these uncertainties in our final estimate is to run a Monte-Carlo simulation. For each simulation, we iterate over all 11 candidates in our sample and include  $P_1(x)$  number of sources in that trial with a  $UV$  luminosity equal to that candidate – where  $P_1(x)$  is a Poisson distribution with mean equal to 1. Then, we run over all the sources and give each source 10-20% chance of being thrown out (to account for uncer-



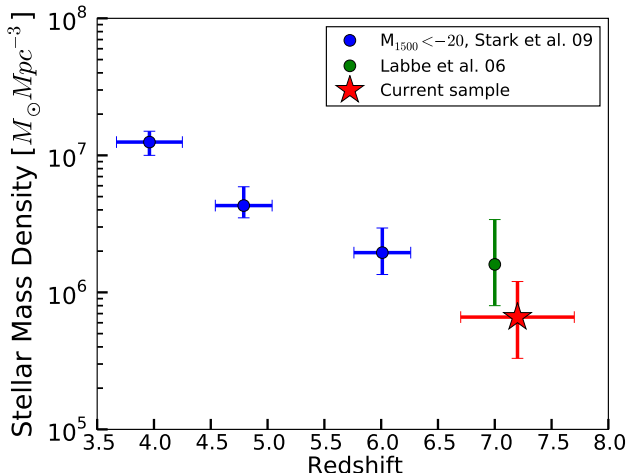


FIG. 6.— The stellar mass density as a function of redshift. Our estimate of the stellar mass density at  $z \sim 7$  is shown with the red star and considers the contributions from galaxies with absolute magnitudes  $M_{UV,AB} < -20$ . The horizontal error bars show the approximate width of our samples in redshift space. Also shown are the stellar mass density determinations of Stark et al. 2009 at  $z \sim 4$ ,  $z \sim 5$ , and  $z \sim 6$  (blue points). The green point at  $z \sim 7$  is from Labbé et al. 2006. That estimate was derived from two  $z \sim 7$  candidates in the HUDF identified by Bouwens et al. (2004c). Those candidates are also included in this study. The limiting UV luminosity probed by our sample is comparable to the points at lower redshift.

tainties in the contamination fraction). Next, we assign a mass to each of the objects in the particular realization by drawing a random  $M/L_{UV}$  from the observed values. When doing this, we also include individual uncertainties in the  $M/L_{UV}$  determinations, specifically, we make a weighted choice of a mass from the distribution associated to a particular source (with the weights derived from the  $\chi^2$  as was already described for the determination of the ages). Finally, we divide each source by the selection volume appropriate to its  $UV$  luminosity and sum the sources to calculate the stellar mass density for a given trial. We repeated the simulation 10000 times to ensure that our results were not limited by the number of trials. After sorting the distribution, we found that the 68% upper and lower limits on the stellar mass density were  $3.3 \times 10^5 M_{\odot} \text{Mpc}^{-3}$  and  $1.2 \times 10^6 M_{\odot} \text{Mpc}^{-3}$ , respectively.

*Summary:* Above we derive three different estimates of the stellar mass densities with uncertainties. The estimates are  $5.7$ ,  $4.5$ , and  $6.6^{+5.4}_{-3.3} \times 10^5 M_{\odot} \text{Mpc}^{-3}$ . All these estimates are consistent with each other but we prefer the random  $M/L$  approach because this one should be less affected by possible systematic errors in the mass derived from poor photometry. We present this stellar mass density in Figure 6 and show the previous determinations of Stark et al. (2009) at  $z \sim 4-6$  and Labbé et al. (2006) at  $z \sim 7$  for context. We discuss differences between these stellar mass density determinations and the observed trends in §8 and §9. We should also note here that allowing moderate extinction ( $A_V < 0.5$ ) produces SMD measurements that are fully consistent with the previous values (within the uncertainties).

### 7.3. SFR Density Determinations

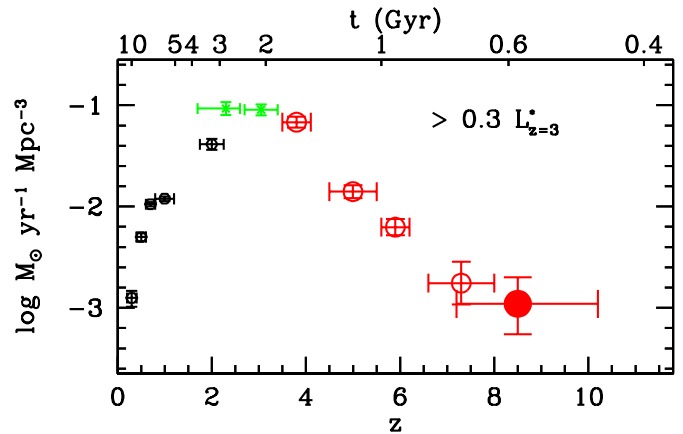


FIG. 7.— The approximate star formation rate density inferred at  $z \sim 8.5$  (solid red circle) by combining the age constraints we have on  $z \sim 7$  galaxies with the stellar mass density we estimate (§7.3). For our estimated SFR density, we use the stellar mass density we derive at  $z \sim 7$  divided by the average age of our sample. Included on this figure are the dust-corrected SFR density determinations at  $z \sim 7$  from  $z \sim 7$   $z$ -dropout search (Bouwens et al. 2008: *open red circle*), the Bouwens et al. (2007) determination at  $z \sim 4-6$  (*open red circles*), the Reddy & Steidel (2009) determinations at  $z \sim 2-3$  (*green crosses*), and the Schiminovich et al. (2005) determinations at  $z \lesssim 2$  (*black hexagons*). Dust corrections are as in Bouwens et al. (2009a).

The advantage of the current stellar population modeling is that it permits to estimate the SFR in our candidates at even earlier times. Combining our age constraints with the estimated SMD we can place limits on the SFR density at even earlier times.

In terms of the previous history, the constant SF models imply ages of the galaxies consistent with them being in place at around  $z \sim 10$ , which combined with their assembled masses imply a very simple estimate of the average SFRD between  $7 < z < 10$ . The amount of time elapsed corresponds to 300 Myr and the stellar mass assembled in that amount of time is  $3.3 \times 10^5 M_{\odot} \text{Mpc}^{-3}$ . This implies a SFRD of  $1.1 \times 10^{-3} M_{\odot} \text{yr}^{-1} \text{Mpc}^{-3}$  (see Figure 7). An extreme approach that would maximize the SFRD comes from the single burst models. Simply dividing the total masses ( $6.6 \times 10^5 M_{\odot} \text{Mpc}^{-3}$ ) by the ages of the sources (80 Myr for the single burst models) yields an average SFRD of  $8 \times 10^{-3} M_{\odot} \text{yr}^{-1} \text{Mpc}^{-3}$  in the previous 80 Myr.

## 8. RELIABILITY OF CURRENT RESULTS

### 8.1. Comparison with Previous Photometry

In general, our optical to near-IR photometry is consistent with the photometry presented in Bouwens et al. (2009, in preparation) although a systematic offset of  $\sim 0.2$  magnitudes is present due to the fact that the fluxes presented there were measured in a somewhat smaller aperture and no aperture corrections were applied. We also find excellent agreement between the mid-IR IRAC fluxes measured for our HUDF  $z$ -dropouts and those presented in Labbé et al. (2006). Although this might not be surprising due to our use of the same technique for doing photometry, our modeling of the flux from neighboring sources (and subsequent removal of this flux) is completely independent. This illustrates the robustness of our method for doing photometry. An in-

dependent test of the quality of photometry can be obtained by comparing flux measurements for sources with deep IRAC observations taken in both GOODS epochs (rotated by 180 degrees). In general, we observe excellent agreement between the two measurements for the five sources with two epoch data (the four UDF  $z$ -dropouts and CDFS-3225-4627) – suggesting that systematics are minimal. The only exception to this is for the  $3.6 \mu\text{m}$  measurement for GNS- $z$ D2, GNS- $z$ D5, and HDFN-3654-1216 where there are bright nearby neighbors.

### 8.2. Comparison with Previous Estimates of the Stellar Mass Density at $z \sim 7$

Previously, Labbé et al. (2006) made an estimate of the stellar mass density at  $z \sim 7$  based upon a small (4 galaxy) HUDF  $z$ -dropout sample. They estimated a stellar mass density of  $1.6_{-0.8}^{+1.8} \times 10^6 M_{\odot} \text{Mpc}^{-3}$  to  $>0.3 L_{z=3}^*$ . Since we adopt a similar limiting luminosity, we can make a direct comparison with the stellar mass density estimated here. We find a fiducial value that is about half the one estimated by Labbé et al. (2006). This is mostly due to our different choice of star formation histories (we favor constant SF histories versus the average between SSP and constant SFR used in that work). These estimates are fully consistent within the uncertainties.

This quantity was also estimated by Stark et al. (2009) at  $z \sim 4 - 6$  for sources in the GOODS fields to similar depth (see figure 6). A simple calculation shows that the observed growth in mass between  $z \sim 7$  and  $z \sim 6$  is consistent with the observed SFRD derived from the UV LF studies of Bouwens et al. (2008).

### 8.3. How Significant Is Crowding for Current Samples

Because of the broad PSF in IRAC data, crowding is considered to be a potentially significant concern in doing photometry on faint sources, particularly when these sources are nearby bright foreground galaxies. In fact, in many studies, it is thought that perhaps  $\sim 50\%$  of faint sources are sufficiently close to their neighbors that IRAC photometry is impossible. What do we find here?

We attempted to do IRAC photometry on all 11  $z$ -dropouts in the Bouwens et al. (2009, in preparation), without excluding any sources due to crowding issues. Of the 11 sources presented here, 5 suffered significant blending with nearby neighbors. However, as a result of our deblending technique (Labbé et al. 2006), we were able to recover reliable fluxes for all 11 in the  $4.5 \mu\text{m}$  band and 8 of 11 (73%) in the  $3.6 \mu\text{m}$  band (excluding GNS- $z$ D2, GNS- $z$ D5, and HDFN-3654-1216 which showed strong residuals from the neighbors after the subtraction process – implying large systematic errors in those two cases). This agrees with Monte-Carlo experiments that we performed that suggest that photometry is possible for  $\gtrsim 80\%$  of faint sources and that the largest errors in the recovered fluxes should be roughly a factor of 2.

## 9. DISCUSSION

### 9.1. Stellar mass growth during the first Gyr of the Universe.

Despite the large uncertainties in the derived individual masses, it seems clear now that quite massive

( $> 10^{10} M_{\odot}$ ) systems with evolved stellar populations were already present in the universe at very early times ( $z \sim 7$  or at least  $z \sim 6$ ). These very massive systems likely correspond with the most massive Dark Matter Haloes (DMH) and are predicted to exist but in low numbers in the standard Press Schechter formalism. It is hard to run simulations that can probe this very massive end of the Mass function since to obtain them in larger numbers it would be necessary to run simulations with quite large volumes. Davé et al. (2006) ran an SPH simulation with a comoving volume of  $10^5 \text{Mpc}^3$  which they find to be adequate to probe the stellar mass range  $10^{7.2} - 10^{10} M_{\odot}$ . At the median mass of our sample of  $5 \times 10^9 M_{\odot}$ , they find a number density of  $\sim 10^{-4} \text{Mpc}^{-3}$ . More recently, Choi & Nagamine (2009, in preparation), ran a simulation in a larger box of  $\sim 3 \times 10^6 \text{Mpc}^3$  and find the number density at  $5 \times 10^9 M_{\odot}$  to be approximately one half that predicted by Davé et al. (2006). Given the uncertainties, these predictions agree quite well with the density of such objects that we find of  $1.6 \times 10^{-4} \text{Mpc}^{-3}$ . Although our sample may still suffer from small number statistics, the fact is that such massive objects are found to be fairly common at this early epochs and their moderately evolved SEDs show that their stellar populations are not pristine but were partly formed at higher redshifts.

### 9.2. Star Formation Histories of high redshift galaxies.

It is well known that the results (e.g., derived masses, SFRs, etc.) of stellar population analyses can depend significantly on the functional form one assumes for the star formation history. Some care, therefore, needs to be given to the parameterization of these histories to ensure that the conclusions drawn do not depend too much on artifacts of this parameterization.

To illustrate, there are 3 different model parameterizations of the star formation history in common use in the literature: instantaneous burst models, exponentially decay star formation models, and constant star formation models. Instantaneous burst models give younger ages and lower masses than exponential decay models which in turn give younger ages and lower masses than constant star formation models. The instantaneous burst models do not seem realistic but are useful to set lower limits on the derived ages and masses. Exponential decay models are the most popular in the literature (e.g. Yan et al. 2006; Eyles et al. 2007; Stark et al. 2009) – perhaps because of their versatility in modeling a wide range in star formation histories – but give rise to a troubling prediction, namely, that the star formation rates of galaxies are larger in the past. This prediction is troubling because it contradicts both the observed and predicted trend that the SFR density of the universe increases with cosmic time.

Given these concerns, we prefer to model the stellar population of high-redshift galaxies with constant star formation histories. The reason for this preference is as follows: first, constant star formation models do not naturally predict that the SFR density will be greater at early times, as exponentially decaying models do. Second, constant star formation models do not predict a large population of UV luminous sources at earlier times as found from exponentially-decaying models (e.g.,

TABLE 4  
KEY RESULTS DERIVED FROM  $z \sim 7$  SAMPLE.

Quantity	Value
Redshifts	$7.2 \pm 0.5$
Masses	$0.1\text{-}12 \times 10^9 M_\odot$
$M/L_{UV}$ ratio	$0.01\text{-}0.1 M_\odot/L_\odot$
Minimum Age <sup>a</sup>	80 Myr
Average Age	300 Myr
$UV$ -continuum Slope $\beta$	$-2.4 \pm 0.4$
Specific SFR	$2.4 \pm 0.6 \text{ Gyr}^{-1}$
Mass Density (Direct)	$5.7 \times 10^5 M_\odot \text{ Mpc}^{-3}$
Mass Density (M/L of Mean SED)	$4.5 \times 10^5 M_\odot \text{ Mpc}^{-3}$
Mass Density (Random M/L) <sup>b</sup>	$6.6_{-3.3}^{+5.4} \times 10^5 M_\odot \text{ Mpc}^{-3}$
Predicted SFR density (at $z = 9$ )	$0.0011 M_\odot \text{ yr}^{-1} \text{ Mpc}^{-3}$

<sup>a</sup> From single burst models.

<sup>b</sup> Our best estimate.

Yan et al. 2006). This is more consistent with the observation that such sources are not found in large numbers at  $z \sim 7$ . Third, constant star formation models are more consistent with the low evolution seen in the specific star formation rate (e.g., Figure 5 here, §6.2, and as discussed by Stark et al. 2009). We realize that *some* luminous galaxies may have mass-to-light ratios suggesting their SFRs were higher in the past, but we suspect this may be a duty cycle issue that is due to feedback, etc. These galaxies are simply experiencing a period where their SFRs are less than their norm.

### 9.3. Reionization

As outlined in §7.3, the stellar population modeling we do of  $z \sim 7$  galaxy candidates allow us to estimate the SFR density at even earlier times. Having an estimate of this SFR density is valuable since it allows us to assess how much ionizing radiation the star-forming population at  $z \gtrsim 7$  might likely produce – and hence reposes the question about whether  $z \gtrsim 6$  galaxies are capable of keeping the universe reionized. From absorption studies to bright  $z \sim 6$  QSOs, the process of reionizing the hydrogen of the universe was just ending at  $z \sim 6$  (Fan et al. 2006; Becker et al. 2001) while the five year WMAP results suggest it began at least as early as  $z \sim 11$  (Komatsu et al. 2009).

Madau et al. (1999) presented a prescription to estimate the critical density of UV radiation necessary to reionize the universe at a given redshift. Updated to a more current cosmology (Komatsu et al. 2009), that formula becomes:

$$\rho_{SFR}^{crit}(z) \approx \frac{0.04}{f_{esc}} \left( \frac{1+z}{8} \right)^3 \left( \frac{C}{30} \right) \left( \frac{\Omega_b h_{70}^2}{0.0463} \right)^2 M_\odot \text{ yr}^{-1} \text{ Mpc}^{-3} \quad (1)$$

At  $z = 7$ , for an escape fraction  $f_{esc} = 0.1$  (e.g. Shapley et al. 2006), and for a clumping factor  $C = 30$  (but see Pawlik et al. 2009 who suggest  $C \sim 6$ ) the value of  $\rho_{SFR}^{crit} = 0.4 M_\odot \text{ yr}^{-1} \text{ Mpc}^{-3}$ . The sources capable of producing such radiation, however, remain unknown but young O and B stars in early galaxies stand out as the most likely candidates given the observed decrease in the number density of quasars at high redshifts.

Based upon the stellar mass density and the mean ages we derive in §6 and §7 for the sample, we estimated an average SFR density of  $0.0011 M_\odot \text{ yr}^{-1} \text{ Mpc}^{-3}$  between

$7 < z < 10$  (§7.3). This is more than 2 orders of magnitude below the SFR density required to reionize the universe at  $z = 7$ . We can also obtain an upper limit to the SFR density by considering the minimal ages obtained from the single burst models. The mean age of 80 Myr obtained from these models implies a SFR density of  $0.008 M_\odot \text{ yr}^{-1} \text{ Mpc}^{-3}$  at  $z = 8$  (§7.3). Even for this larger value for the SFR density, we are still a factor  $\sim 50$  below that required to reionize the universe. Of course, these values are based only on the brightest observable sources and so including the mass from galaxies of even lower luminosities than our selection limit would increase these numbers by a factor of  $\gtrsim 2 - 3$ . In any case, it bears mention that we cannot include the contribution from a population of dust obscured sources that we would miss in LBG selections. However, as we have already noted in §6.1 and §6.2 there is strong evidence that the contribution from this population is not large (e.g., Bouwens et al. 2009a).

## 10. SUMMARY

We use the very deep optical, near-IR, and IRAC data over and around the two GOODS fields to study the properties of a large sample of  $\sim 11$   $z$ -dropout galaxies at  $z \sim 7$ . Considered are the ages, stellar masses, redshifts, and dust properties of  $z \sim 7$  galaxies. The  $z$ -dropout candidates were drawn from the very large selection of such galaxies from  $\sim 80$  arcmin<sup>2</sup> of deep NICMOS data by Bouwens et al. (2009, in preparation). Essential to this analysis is the availability of deep Spitzer IRAC mid-IR data that give us deep coverage of these sources at rest-frame optical wavelengths and hence permits us to estimate the stellar mass. The stellar population modeling was performed with the Bruzual & Charlot (2003) spectral synthesis modeling code with a Salpeter IMF and assuming solar metallicity. We have quantified how our best-fit properties would change, as a function of the assumed IMF and metallicity.

Our conclusions are as follows:

- Photometric redshifts place the candidates at  $6.2 < z < 8.0$  with the mean redshift of the sample at 7.2. The uncertainties in the redshift for individual candidates are typically  $\Delta z \sim 0.5$  and have been taken into account in the derivation of the confidence intervals for the rest of the properties (see §5 and figure 2).
- We use the results of Bouwens et al. (2009a) regarding the low extinctions expected at high redshifts to help us better constrain the individual ages of the sources. Our CSF model fits yield SFRs that are consistent with simple conversion based on the  $L_{1500}$  luminosities. The best-fit ages allow enough time to assemble their masses by the redshift of observation. This does not seem to be the case for the most massive sources in the work by Yan et al. (2006). We argue that this is not likely an effect of large extinctions but rather that these sources are the result of some other more complicated history probably involving mergers (§9.2).
- The star formation history weighted ages of the observed stellar population we derive are in the range



of 170 – 420 Myr with a mean of 300 Myr (there is an outlier with  $\sim 20$  Myr). These ages are consistent with previous work that place the formation of the most massive galaxies at very early epochs. In particular, the bulk of the stars in some of these sources seem to have formed as early as  $z \sim 10$  (see §6 and table 3).

- The stellar masses we estimate for individual  $z \sim 7$   $z$ -dropouts in our sample range from  $0.2 \times 10^9 M_\odot$  to  $12 \times 10^9 M_\odot$ , with a mean for the sample of  $5.1 \times 10^9 M_\odot$ . The masses we estimate are much more well constrained than other quantities – like the age – but are nevertheless still uncertain at the factor of 2 level (§6 and table 3).
- We find that the specific SFRs (SFR/Mass) of the sources in the sample range from  $1.8 \text{ Gyr}^{-1}$  to  $25 \text{ Gyr}^{-1}$ , with a biweight mean value of  $2.4 \pm 0.6 \text{ Gyr}^{-1}$ . We observe that at comparable masses, the specific SFR is surprisingly close to all the values in the literature between  $z \sim 2$  and  $z \sim 6$  (Reddy et al. 2006; Papovich et al. 2001; Daddi et al. 2007; Stark et al. 2009). The constancy of this quantity between  $z \sim 2 - 7$ , in contrast with its fast decline at  $z \lesssim 2$  (Noeske et al. 2007), suggests that star formation proceeds in different ways in these two regimes (see §6.3 and figure 5).
- Utilizing the estimated selection volumes for the Bouwens et al. (2009, in prep)  $z$ -dropout search, we derive the stellar mass density at  $z = 7$  using an approach that randomly samples the M/L of the galaxies with the most reliable IRAC photometry. We find  $6.6_{-3.3}^{+5.4} \times 10^5 M_\odot \text{ Mpc}^{-3}$ . The random M/L approach is preferred as it is less affected by possible systematic errors in photometry. We tested other approaches, including averaging the direct fits, yielding very similar answers. Our estimate of the global stellar mass assembled is consistent with the growth expected based on the SFRD measured between  $6 < z < 7$  and the SMD measured to similar depths at  $z \sim 6$  (§7.2).
- Combining the estimated ages and total assembled mass we can derive an average SFR between  $z \sim 10$  and  $z \sim 7$  of  $1.1 \times 10^{-3} M_\odot \text{ yr}^{-1} \text{ Mpc}^{-3}$ . SSP models provide us with minimum age estimates that in combination with the masses allow us to place

an upper limit to the SFRD at  $z \sim 8$ . This estimate is still a factor 50 below the necessary value to reionize the universe at this redshift (following the Madau et al. 1999 prescription with  $f_{esc} = 0.1$  and  $C = 30$ , eq. 1), in agreement with previous works. We emphasize that this estimate is only based on the most luminous sources and is probably missing most of the UV light, which is being produced by sources in the faint end of the LF (e.g., Bouwens et al. 2007; Reddy & Steidel 2009; Yan & Windhorst 2004).

The Bouwens et al. (2009, in prep) search based on a large area of high quality optical to NIR data has provided us with the first sizable sample of candidate sources at  $z \sim 7$ , a step of 200 Myr with respect to the previous efforts (but see also new work by Oesch et al. 2009b; Bouwens et al. 2009b; McLure et al. 2009b; Bunker et al. 2009; Ouchi et al. 2009). Complementing these data with very deep mid-IR Spitzer IRAC imaging we have been able to fit BC03 SSP models to estimate the masses and ages of galaxies at  $z \sim 7$ . Our results suggest that these galaxies had been forming stars for  $\gtrsim 200$  Myr and as soon as  $z \sim 9-10$ , well into the reionization epoch. We expect to substantially improve upon these results taking advantage of the deep near-IR data soon to become available over the HUDF and CDF-South GOODS field as a result of the new WFC3 instrument on HST. Not only will we substantially increase the number of  $z \sim 7 - 8$  galaxies known, but the deeper data and improved set of near-IR filters ( $Y, J, H$ ) will enable us to perform much more accurate stellar population modeling on individual sources.

We would like to thank the referee for his/her very detailed and insightful report. It has helped us to greatly improve the presentation of our work. We would also like to show our appreciation to Ken Nagamine and Junhwan Choi for giving us early access to the latest results from his simulations. We also acknowledge useful discussions with Daniel Stark. V.G. is gratefully for the support from a Fulbright-CONICYT scholarship. This work is based, in part, on observations made with the Spitzer Space Telescope, which is operated by the Jet Propulsion Laboratory, California Institute of Technology under a contract with NASA. We acknowledge the support of NASA grant NAG5-7697.

#### APPENDIX

Table 2, in the main text, summarizes the photometry for the sample in the usual AB magnitude system. Since this is a  $z$ -dropout sample, most of the optical measurements correspond to upper limits which makes it hard to reproduce the stellar population modeling results presented in this work. In table 5 of this appendix we provide an equivalent table with the actual flux measurements in physical units.

#### REFERENCES

- Becker, R. H., et al. 2001, *AJ*, 122, 2850  
 Beckwith, S. V. W., et al. 2006, *AJ*, 132, 1729  
 Bertin, E., & Arnouts, S. 1996, *A&AS*, 117, 393  
 Bouwens, R. J., Illingworth, G. D., Blakeslee, J. P., & Franx, M. 2006, *ApJ*, 653, 53  
 Bouwens, R. J., et al. 2009a, *ApJ*, 705, 936  
 Bouwens, R. J., Illingworth, G. D., Franx, M., & Ford, H. 2007, *ApJ*, 670, 928  
 —. 2008, *ApJ*, 686, 230  
 Bouwens, R. J., et al. 2009b, submitted, arXiv:0909.1803  
 —. 2004c, *ApJ*, 616, L79



TABLE 5  
SUMMARY OF PHOTOMETRY.

ID	$B_{435}$	$v_{606}$	$i_{775}$	$z_{850}$	$J_{110}$	$H_{160}$	$K_s$	$3.6\mu\text{m}$	$4.5\mu\text{m}$
UDF-640-1417	0.18±0.41	-0.22±0.26	-0.07±0.41	2.88±0.63	8.91±1.37	13.13±2.11	17.49±3.14	30.88±3.51	16.75±6.88
UDF-983-964	-0.37±0.41	-0.07±0.26	-0.30±0.44	0.04±0.74	7.77±1.37	7.06±1.66	8.25±4.66	12.06±3.51	8.21±6.88
UDF-387-1125	-0.07±0.37	0.04±0.22	-0.04±0.37	0.85±0.63	3.11±1.04	6.32±1.63	2.03±4.07	2.96±3.55	0.07±6.99
UDF-3244-4727	-0.41±0.37	-0.22±0.26	-0.74±0.37	-0.59±0.67	3.48±1.07	6.32±1.78	-1.26±5.51	9.47±3.55	7.40±6.92
GNS-zD1	-0.78±1.33	-0.74±0.89	-0.30±1.78	1.33±2.48	9.32±2.29	12.50±2.55	...	40.20±5.07	26.11±9.69
GNS-zD2	-0.41±1.04	0.89±0.81	-2.29±1.59	1.29±1.59	5.66±1.96	7.73±2.48	...	9.84±5.33	11.87±9.80
GNS-zD3	-0.55±0.85	0.33±0.67	-0.33±0.96	0.44±1.26	4.25±2.66	7.73±2.33	...	18.97±5.07	15.87±9.65
GNS-zD4	-0.15±1.48	-0.11±1.07	-1.04±1.59	1.41±1.63	7.58±2.48	11.13±3.00	...	31.36±4.77	26.70±10.21
GNS-zD5	-0.33±1.07	0.11±0.81	-1.89±1.22	2.15±1.41	11.76±3.37	28.18±3.48	24.59±4.07	52.74±3.66	25.78±7.06
CDFS-3225-4627	0.78±1.26	0.59±0.92	-2.77±1.33	1.59±1.63	6.77±2.37	9.76±2.70	...	13.24±3.55	14.68±7.06
HDFN-3654-1216	-1.26±0.74	0.59±0.67	1.11±1.33	9.21±1.89	12.39±2.55	15.94±2.22	10.02±3.40	30.18±6.99	19.45±11.80

NOTE. — Photometry for the sample. Fluxes are in units of 10 nJy. This table is equivalent to table 2 but here we present the actual flux measurements in the optical instead of tabulating the  $1\sigma$  upper limits.

- Bouwens, R. J., Illingworth, G. D., Blakeslee, J. P., Broadhurst, T. J., & Franx, M. 2004b, *ApJ*, 611, L1  
 Bouwens, R. J., et al. 2010, *ApJ*, 708, L69  
 Bradley, L. D., et al. 2008, *ApJ*, 678, 647  
 Brammer, G. B., van Dokkum, P. G., & Coppi, P. 2008, *ApJ*, 686, 1503  
 Brinchmann, J., & Ellis, R. S. 2000, *ApJ*, 536, L77  
 Bruzual, G., & Charlot, S. 2003, *MNRAS*, 344, 1000  
 Bunker, A., et al. 2009, submitted, arXiv:0909.2255  
 Bunker, A. J., Stanway, E. R., Ellis, R. S., & McMahon, R. G. 2004, *MNRAS*, 355, 374  
 Calzetti, D., Armus, L., Bohlin, R. C., Kinney, A. L., Koornneef, J., & Storchi-Bergmann, T. 2000, *ApJ*, 533, 682  
 Castellano, M., et al. 2009, submitted, arXiv:0909.2853  
 Daddi, E., et al. 2007, *ApJ*, 670, 156  
 Davé, R., Finlator, K., & Oppenheimer, B. D. 2006, *MNRAS*, 370, 273  
 Dickinson, M. 1999, in *IAP Conference Proceedings, Vol 470, After the Dark Ages: When Galaxies were Young (the Universe at 2  $\%Z \geq 5$ )*, ed. S. Holt E. Smith, 122  
 Egami, E., et al. 2005, *ApJ*, 618, L5  
 Erb, D. K., Steidel, C. C., Shapley, A. E., Pettini, M., Reddy, N. A., & Adelberger, K. L. 2006, *ApJ*, 646, 107  
 Eyles, L. P., Bunker, A. J., Ellis, R. S., Lacy, M., Stanway, E. R., Stark, D. P., & Chiu, K. 2007, *MNRAS*, 374, 910  
 Eyles, L. P., Bunker, A. J., Stanway, E. R., Lacy, M., Ellis, R. S., & Doherty, M. 2005, *MNRAS*, 364, 443  
 Fan, X., et al. 2006, *AJ*, 132, 117  
 Fazio, G. G., et al. 2004, *ApJS*, 154, 10  
 Ferguson, H. C., et al. 2004, *ApJ*, 600, 107  
 Fioc, M., & Rocca-Volmerange, B. 1997, *A&A*, 326, 950  
 Giavalisco, M., et al. 2004, *ApJ*, 600, L93  
 Hickey, S., Bunker, A., Jarvis, M. J., Chiu, K., & Bonfield, D. 2009, submitted, arXiv: 0909.4205  
 Kajisawa, M., et al. 2006, *PASJ*, 58, 951  
 Komatsu, E., et al. 2009, *ApJS*, 180, 330  
 Kriek, M., van Dokkum, P. G., Labbé, I., Franx, M., Illingworth, G. D., Marchesini, D., & Quadri, R. F. 2009, *ApJ*, 700, 221  
 Labbé, I., Bouwens, R., Illingworth, G. D., & Franx, M. 2006, *ApJ*, 649, L67  
 Labbé, I., et al. 2003, *AJ*, 125, 1107  
 —. 2007, *ApJ*, 665, 944  
 Labbe, I., et al. 2010, *ApJ*, 708, L26  
 Lehnert, M. D., & Bremer, M. 2003, *ApJ*, 593, 630  
 Madau, P., Haardt, F., & Rees, M. J. 1999, *ApJ*, 514, 648  
 Madau, P., Pozzetti, L., & Dickinson, M. 1998, *ApJ*, 498, 106  
 Maiolino et al. 2008, *A&A*, 488, 463  
 Maraston, C. 2005, *MNRAS*, 362, 799  
 McLure, R. J., Cirasuolo, M., Dunlop, J. S., Foucaud, S., & Almaini, O. 2009a, *MNRAS*, 395, 2196  
 McLure, R. J., Dunlop, J. S., Cirasuolo, M., Koekemoer, A. M., Sabbi, E., Stark, D. P., Targett, T. A., & Ellis, R. S. 2009b, submitted, arXiv: 0909.2437  
 Mobasher, B., et al. 2005, *ApJ*, 635, 832  
 Noeske, K. G., et al. 2007, *ApJ*, 660, L43  
 Oesch, P. A., et al. 2009a, submitted, arXiv:0909.1806  
 —. 2009b, *ApJ*, 690, 1350  
 —. 2009d, arXiv:0909:5183  
 Oke, J. B., & Gunn, J. E. 1983, *ApJ*, 266, 713  
 Ouchi, M., et al. 2009, submitted, arXiv:0908.3191  
 Ouchi, M., Tokoku, C., Shimasaku, K., & Ichikawa, T. 2007, *Cosmic Frontiers ASP Conference Series*, 379, 47  
 Papovich, C., Dickinson, M., & Ferguson, H. C. 2001, *ApJ*, 559, 620  
 Pawlik, A. H., Schaye, J., & van Scherpenzeel, E. 2009, *MNRAS*, 394, 1812  
 Peng, C. Y., Ho, L. C., Impey, C. D., & Rix, H.-W. 2002, *AJ*, 124, 266  
 Reddy, N. A., & Steidel, C. C. 2009, *ApJ*, 692, 778  
 Reddy, N. A., Steidel, C. C., Fadda, D., Yan, L., Pettini, M., Shapley, A. E., Erb, D. K., & Adelberger, K. L. 2006, *ApJ*, 644, 792  
 Salpeter, E. E. 1955, *ApJ*, 121, 161  
 Sawicki, M., et al. 2007, *At the Edge of the Universe: Latest Results from the Deepest Astronomical Surveys ASP Conference Series*, 380, 433  
 Sawicki, M., & Yee, H. K. C. 1998, *AJ*, 115, 1329  
 Schiminovich, D., et al. 2005, *ApJ*, 619, L47  
 Shapley, A. E., Steidel, C. C., Pettini, M., Adelberger, K. L., & Erb, D. K. 2006, *ApJ*, 651, 688  
 Stanway, E. R., Bunker, A. J., & McMahon, R. G. 2003, *MNRAS*, 342, 439  
 Stanway, E. R., McMahon, R. G., & Bunker, A. J. 2005, *MNRAS*, 359, 1184  
 Stark, D. P., Bunker, A. J., Ellis, R. S., Eyles, L. P., & Lacy, M. 2007, *ApJ*, 659, 84  
 Stark, D. P., Ellis, R. S., Bunker, A., Bundy, K., Targett, T., Benson, A., & Lacy, M. 2009, *ApJ*, 697, 1493  
 Thompson, R. I., et al. 2005, *AJ*, 130, 1  
 Thompson, R. I., Storrie-Lombardi, L. J., Weymann, R. J., Rieke, M. J., Schneider, G., Stobie, E., & Lytle, D. 1999, *AJ*, 117, 17  
 Wilkins, S. M., Bunker, A. J., Ellis, R. S., Stark, D., Stanway, E. R., Chiu, K., Lorenzoni, S., & Jarvis, M. J. 2009, submitted, arXiv:0910.1098  
 Williams, R. E., et al. 1996, *AJ*, 112, 1335  
 Wuyts, S., et al. 2007, *ApJ*, 655, 51  
 Yan, H., Dickinson, M., Giavalisco, M., Stern, D., Eisenhardt, P. R. M., & Ferguson, H. C. 2006, *ApJ*, 651, 24  
 Yan, H., et al. 2005, *ApJ*, 634, 109  
 Yan, H., Windhorst, R., Hathi, N., Cohen, S., Ryan, R., O'Connell, R., & McCarthy, P. 2009, submitted, arXiv:0910.0077  
 Yan, H., & Windhorst, R. A. 2004, *ApJ*, 600, L1  
 Yoshida, M., et al. 2006, *ApJ*, 653, 988  
 Zheng, W., et al. 2009, *ApJ*, 697, 1907